Lab on a Chip

PAPER

Published on 01 October 2025
Licence and permissions

Cite this: *Lab Chip*, 2025, **25**, 5875

Building multiple microenvironmental niches using a customizable 3D printed well insert

Laura A. Milton,[abc] Surasak Kasetsirikul,[ab] Jorge A. Catano,[ab] F. Sofia Hilmi,[abf] Zeheng Zhou,[de] Thomas G. Molley,[dk] Kristopher A. Kilian,[dek] Louis J. Y. Ong,[abgj] James Chirnside,[a] Nicholas Byrom,[a] Georgia Balshaw,[a] Sammy Liang,[a] Laura J. Bray,[abf] Dietmar W. Hutmacher,[bfgh] Christoph Meinert[bc] and Yi-Chin Toh *[abfgi]

The increasing demand for advanced *in vitro* models that replicate physiological crosstalk between cell types within and between organs requires customized cellular microenvironments arranged within a single platform. Hydrogels are biomaterials that mimic the physicochemical properties of tissue niches to optimally support diverse cell types. However, they require integration with cell patterning platforms like bioprinting or microfluidics to create organized multi-niche environments. There is currently a gap between bioprinting, which is scalable but limited by availability of printable hydrogels, and microfluidic patterning, which is compatible with diverse biomaterials but is challenging to multiplex. Here, we developed the Localized Microenvironment Well-Insert (LM-Well), a 3D-printed device designed to pattern multiple hydrogel niches with customizable physicochemical properties in multi-well plates. The LM-Well features patterning structures that enable capillary force-driven patterning of various hydrogel formulations, including natural, photo-crosslinkable and synthetic click hydrogels. Functional materials, exemplified by oxygen-scavenging microcapsules, can be patterned within the LM-Well offering an additional layer of control over local oxygen levels in individual cell niches, which modulated tumor growth and zonation of hepatic activities. Micro-architectural supports, such as micropillars or scaffolds, can be integrated into the LM-Well to optimally support mechanically-active cells like myocytes. The LM-Well's multi-niche patterning capability enabled the establishment of a liver-tumor co-culture in a single well, recapitulating altered drug efficacy on MCF-7 tumor cells following activation of tamoxifen and deactivation of doxorubicin by HepaRG-derived hepatocytes. As a versatile and accessible platform, the LM-Well facilitates physiologically relevant co-cultures with customizable niches and diverse biomaterials.

Received 31st July 2025,
Accepted 22nd September 2025

DOI: 10.1039/d5lc00753d

rsc.li/loc

1. Introduction

In vitro study of normal and pathological physiology requires recapitulating the complex crosstalk between multiple cell types within and across organ systems, as tissues function as interconnected networks.[1,2] To replicate this complexity in experimental models, it is crucial to engineer cellular microenvironments that are tissue-specific and capable of dynamic interactions. Each microenvironment must be precisely designed to meet its associated cell type's unique biochemical and mechanical needs, ensuring proper cell phenotype and function. Moreover, these microenvironments must be spatially organized and structurally patterned to facilitate signal exchange and integration between distinct cell populations. This coordinated design is essential for capturing the interdependent processes that drive tissue physiology.

[a] *Faculty of Engineering, School of Mechanical, Medical and Process Engineering, Queensland University of Technology, Brisbane, 4000, Australia*
[b] *Centre for Biomedical Technologies, Queensland University of Technology, Brisbane, Australia*
[c] *Gelomics Pty Ltd., Kelvin Grove, 4059, Australia*
[d] *School of Materials Science and Engineering, University of New South Wales, Sydney, NSW, 2052, Australia*
[e] *School of Chemistry, Australian Centre for NanoMedicine, University of New South Wales, Sydney, NSW, 2052, Australia*
[f] *ARC Training Centre for Cell and Tissue Engineering Technologies, Queensland University of Technology, Brisbane, 4000, Australia*
[g] *Max Planck Queensland Centre (MPQC) for the Materials Science of Extracellular Matrices, Queensland University of Technology, Brisbane, 4000, Australia*
[h] *Australian Research Council (ARC) Training Centre for Multiscale 3D Imaging, Modelling and Manufacturing (M3D Innovation), Queensland University of Technology, Brisbane, 4000, Australia*
[i] *Faculty of Health, School of Biomedical Sciences, Queensland University of Technology, Brisbane, 4000, Australia*
[j] *School of Applied Sciences, Temasek Polytechnic, Singapore, 529757*
[k] *OxyLo Inc., San Diego, California, USA*

Functional biomaterials, particularly hydrogels, are widely used to design tailored microenvironments for specific cell types due to their highly tunable biochemical and mechanical properties.[3,4] Hydrogels are composed of hydrophilic polymer chains crosslinked into three-dimensional networks.[4,5] The biochemical properties of these materials can be customized by selecting natural (*e.g.* collagen, fibrin, decellularized matrices[6,7]) or synthetic (*e.g.* polyethylene glycol (PEG)) polymers which can be further functionalized to present specific cell adhesion peptides[8] or growth factors[9,10] to augment cell functions. Additionally, hydrogel crosslinking mechanisms can be tailored using techniques such as photopolymerization, thermal gelation, enzymatic crosslinking, click chemistry or ionic interactions[4,5] to allow greater control over their mechanical properties. However, hydrogels must be integrated with a cell patterning platform, such as bioprinting or microfluidic patterning, to precisely organize multiple cell niches within a shared environment to recapitulate multi-cellular interactions.

Bioprinting encompasses a suite of technologies that employ different mechanisms, including extrusion, light polymerization and droplet jetting, to dispense and crosslink cell-laden hydrogels into geometrical structures.[11–13] While it enables the patterning of multi-cell niches in automation-compatible multi-well plates,[14,15] the properties of the hydrogel bioinks must match the working principle of the 3D printing modality. For example, extrusion-based bioprinting demands hydrogels with precise viscosity and mechanical stability;[16] stereolithography and digital light processing (DLP) based printing require photocrosslinkable hydrogels[17–19] and drop-on-demand bioprinting typically requires low viscosity materials with specific surface tensions and small particle sizes.[13,20,21] Most biochemically rich, unmodified natural hydrogels (*e.g.* collagen, Matrigel), which are commonly used to support sensitive primary or stem cells, are often not amenable to bioprinting due to their high viscosity and low mechanical stability.[22,23] These specific material requirements limit bioprinting's ability to tailor diverse microenvironments for multiple cell types in a single platform, especially when different cells require distinct hydrogel properties. For example, parenchymal cells, such as tumor or hepatocytes, require soft gels with Young's moduli in the 200 Pa to 10 kPa range,[24,25] while mechanically active stromal cells, like smooth muscle cells or fibroblasts, often require stiffer hydrogels with Young's moduli in the 10 to 100 kPa range,[26–28] which cannot be easily achieved with the same class of hydrogel.

Microfluidic patterning offers a more versatile method for organizing cell-laden hydrogels, as it is far less dependent on specific material properties. This approach leverages capillary forces between a liquid (*i.e.* the hydrogel prepolymer) and physical structures such as pillars,[29] phase guides[30] and stepped terraces,[31] to precisely control the flow and localization of the hydrogel prepolymer within enclosed microchannels.[32] Once positioned, the hydrogel can be solidified independently through thermal, photochemical, or ionic crosslinking, creating compartmentalized regions containing distinct cell types. Microfluidic patterning has been used in various organ-on-chip (OoC) devices to study crosstalk between tumor, vasculature and immune cells;[33] vasculature and epithelial tissues;[34] and liver, heart and lung cells.[35]

Despite its potential, the adoption of traditional microfluidic devices to pattern multiple cell niches is limited by the need for specialized microfabrication facilities and workflows that are often incompatible with routine biological laboratory practices. These barriers make it challenging for researchers without microfluidic expertise to integrate this technology into their research, restricting broader accessibility and use.[36] To address this limitation, researchers have explored controlling capillary flow in "open" microfluidic systems, where at least one microchannel wall is air.[37–39] This allows for the creation of a new class of well-plate compatible microfluidic devices, which comprise of flat patterning structures that are suspended in open well plates to form an "open" microfluidic channel defined by the patterning structure and the bottom of the well plate.[37,40] Such open microfluidic well-insert devices have been successfully used to pattern hydrogels in tissue culture well plates to support multi-cellular cultures of prostate cancer with adipocytes,[41] or model crosstalk between mammalian, fungal and bacterial cells.[40]

In this study, we enhanced the functionality of open microfluidic patterning devices by leveraging recent advances in stereolithography (SLA) 3D printing, which allows for the fabrication of three-dimensional constructs with high precision.[36,42] This enabled us to design the Localized Microenvironment Well-Insert (LM-Well), a novel open microfluidic device with a form factor of a well-insert. This design ensures easy and accurate placement of patterning structures within multi-well plates, providing a user-friendly and scalable platform. Importantly, this platform does not rely on complex surface treatments to pattern hydrogels in wells, using only a simple insert to guide fluid. Here, we show an embodiment of the LM-Well which had three separate patterning structures, referred to as leaflets, to precisely pattern three distinct hydrogel niches with controllable physicochemical properties across diverse hydrogel classes, including natural, photo-crosslinkable, and synthetic click hydrogels, all within a single 24-well. Compared to traditional microfluidic and OoC platforms, the LM-Well is inexpensive to fabricate, scalable, and designed for straightforward use in routine laboratories without specialized training or equipment. Indeed, owing to its 3D-printed design, additional micro-architectural structures in micropillars or scaffolds can be printed at the base of the leaflets to optimally support the remodeling of cells, such as C2C12 myocytes.

Furthermore, functional biomaterials like oxygen-scavenging microcapsules can be patterned using the LM-Well to control local oxygen levels, enabling applications such as modulating tumor growth or replicating hepatic zonal metabolic activities. These capabilities of the LM-Well facilitated the establishment of co-cultures in this simple and scalable platform, as exemplified by a liver-tumor co-culture model to detect altered drug efficacy on MCF-7 breast cancer tumor cells following activation of tamoxifen and deactivation of doxorubicin by HepaRG-derived

hepatocytes. The LM-Well provides a versatile and easily accessible tool for creating physiologically relevant co-culture systems with tailored niches and various biomaterials.

2. Methods

2.1. LM-Well design

The LM-Well was designed using SolidWorks 2022 (Dassault Systemes) to fit inside a 24-well cell culture plate (Nunc, Thermo Fisher Scientific), with dimensions sourced from the manufacturer. We designed a well insert with three horizontal, flat leaflets suspended above the base of the well, where cell/hydrogel prepolymer solutions can be introduced *via* a circular inlet to the space between the bottom of the leaflets and the base of the well (Fig. 1A). To ensure that large hydrogel volumes (over 30 μL) could be patterned under each leaflet, we designed the leaflets to be as large as possible while fitting in the footprint of the well and leaving a 1 mm allowance around each leaflet to prevent merging. This resulted in three 47.67 mm^2 scalloped triangular leaflets (Fig. 1Aiii), with approximately 10.89 mm wide bases, reaching approximately 6.69 mm into the center of the well. Inlet holes with 2 mm diameter were designed to allow for fluid entry into the vertical gap between the bottom of the leaflets and the bottom of the well (Fig. 1A). To hold the leaflets in place, a central pillar was designed with a stepped, press-fit top lip to fit tightly in the opening of the well plate (Fig. 1A). In addition, the leaflets were designed with trapezoidal edges, wider at the bottom than the top, to prevent capillary rise as previously reported[40] and encourage pinning of the material at the edge of the leaflet by capillary burst effect, which traps liquid at the opening of a sudden expansion, here, the edge of the leaflet expanding to the surrounding well.[43] Print files are supplied in the SI materials.

2.2. 3D printing, post-processing and sterilization

LM-Wells were printed with BioMed Clear resin (FormLabs) on the Form 3B+ printer (FormLabs; reported XY resolution of 25 μm) with a 0.05 mm layer height. Printing parameters included mini-raft supports, a support density of 0.5, and a touchpoint size of 0.3. Post-printing, these devices were rinsed in 100% isopropanol for 5 minutes, followed by sonication in fresh isopropanol for 15 minutes. Post-curing was performed using the FormLabs Form Cure (FormLabs), following the 'BioMed Clear' settings of 60 °C for 1 hour. Inserts were sterilized by submersion in 80% ethanol (w/v) for 2 hours, followed by air-drying in sterile containers at room temperature for 2 days. Inserts were then submerged in sterile phosphate-buffered saline (PBS; Thermo Fisher Scientific) for 2 days at room temperature before being used in cell culture experiments.

2.3. Print fidelity assessment

Print fidelity was assessed using a Nikon BOOM stereomicroscope (Nikon) with measurements compared to computer-aided design (CAD) dimensions. At least 3 devices were measured, each with multiple measurements. Data was represented as percentage error relative to the CAD dimensions.

2.4. Patterning assessments

Patterning of liquids in the LM-Well was assessed qualitatively using food-colored water pipetted into devices with different surface coatings. Approximately 30–40 μL of food-colored water was pipetted into the inlet and pinning was qualitatively assessed – if the water patterned below the leaflets it was deemed successful, if it leaked from the leaflets, it was deemed unsuccessful. Patterning success was assessed dry, with pre-coating in water for 10 minutes, or with pre-coating in 100% fetal bovine serum (FBS; Thermo Fisher Scientific) for 10 minutes. Representative pictographs were collected to demonstrate the patterning success. The volume patterned was assessed by adding food-colored water in 2 μL increments until the leaflet leaked.

2.5. Cell expansion and maintenance

C2C12 mouse myocytes (RRID:CVCL_0188; ATCC) were confirmed to be contamination free and expanded in monolayer culture using high glucose (4.5 g L^{-1}) Dulbecco's Modified Eagle Medium (DMEM; Thermo Fisher Scientific) with 10% FBS and 1% penicillin/streptomycin (Sigma Aldrich) with media changes every two days until 70% confluent. Cells were cultured under standard conditions in a 37 °C, 5% CO_2 humidified incubator.

MCF-7 breast cancer cells (RRID:CVCL_0031; ATCC) were confirmed to be contamination free and expanded in monolayer culture using low glucose (1 g L^{-1}) DMEM (Thermo Fisher Scientific) with 10% FBS, 1% penicillin/streptomycin, 1% sodium pyruvate (Thermo Fisher Scientific; v/v) and 1% minimum essential media non-essential amino acids (MEM-NEAA; Thermo Fisher Scientific; v/v) with media changes every two days until 80% confluent. Cells were cultured under standard conditions in a 37 °C, 5% CO_2 humidified incubator.

HepaRG hepatocytes (RRID:CVCL_9720; Biopredic Advancells) were confirmed to be contamination free and expanded in monolayer culture as previously published[6] using proliferation medium comprising William's E GlutaMAX (Thermo Fisher Scientific), 10% FBS (Thermo Fisher Scientific; v/v), 1% penicillin/streptomycin (Sigma Aldrich; v/v), 50 μM hydrocortisone (STEMCELL Technologies), and 5 μg mL^{-1} insulin (Sigma Aldrich). 6 hours after plating, media was refreshed to eliminate residual dimethyl sulfoxide (DMSO) and subsequently changed every 2–3 days for two weeks. On day 14, cells were passaged. Media replacement continued every 2–3 days until day 28. Starting day 28, differentiation media (proliferation medium containing 1.7% DMSO (Thermo Fisher Scientific; v/v)) was introduced and refreshed every 2–3 days over the next 14 days. On day 42, cells were prepared for encapsulation or plating for assays.

For co-culture media studies, the above MCF-7 and HepaRG media were mixed 1 : 1, for a resultant medium formulation of 50% low glucose DMEM, 50% William's E GlutaMAX with 10% FBS, 1% penicillin/streptomycin, 0.5% sodium pyruvate, 0.5% MEM-NEAA, 25 μM hydrocortisone and 2.5 μg mL^{-1} insulin.

2.6. Cell patterning using the LM-Well

Prior to cell seeding, the LM-Wells were air-dried in a biosafety cabinet. Once dry, the leaflet surfaces were coated with 100% FBS for 10 minutes. Excess FBS was removed using a sterile KimWipe (Kimtech), and the LM-Well was secured into a 24-well plate by applying downward pressure with sterile forceps.

C2C12 (RRID:CVCL_0188; ATCC), MCF-7 (RRID:CVCL_0031; ATCC), and HepaRG (RRID:CVCL_9720; Biopredic Advancells) cells were encapsulated in different hydrogel formulations tailored to their specific requirements. C2C12 cells were encapsulated at 10×10^6 cells per mL in rat tail collagen type 1 (PureCol, 2 mg mL^{-1} final concentration). Collagen was prepared by adding 10× PBS, 1 M sodium hydroxide (NaOH; Sigma Aldrich), and sterile water to the collagen stock. A 15 μL volume of the cell/hydrogel mixture was pipetted into the leaflet of the LM-Well containing pillars. The plate was incubated at 37 °C for 40 minutes to facilitate collagen fibrillogenesis. MCF-7 cells were encapsulated at 1.5×10^6 cells per mL in 5% porcine GelMA with 0.15% LAP photoinitiator (Gelomics). A 20 μL cell/hydrogel suspension volume was pipetted into the LM-Well leaflets and crosslinked for 2 minutes using the LunaCrosslinker (Gelomics). HepaRG were encapsulated at 2×10^6 cells per mL in the previously published liver click dECM hydrogels which have been shown to match physiological liver stiffness (~1.5 kPa) in previous reports.[6] Briefly, cells were mixed with thiolated porcine liver decellularized extracellular matrix (dECM) which was combined with poly-ethylene glycol (PEG) derivatives bound to maleimide groups (JenKem Technologies) to facilitate Michael-type click chemistry in the LM-Well. The 20 μL gels were allowed to polymerize at room temperature for approximately 1–5 minutes. After gel polymerization, 700 μL of the relevant culture medium was added to each well. Crosstalk between the niches is mediated by diffusion of soluble factors between the leaflets within a shared soluble environment. For co-culture studies, the chosen shared co-culture medium was added.

2.7. Live/dead viability staining

Hydrogels were removed, washed with PBS, and stained with 10 μg mL^{-1} Fluorescein Diacetate (FDA; Thermo Fisher Scientific) for live cells and 5 μg mL^{-1} Propidium Iodide (PI; Thermo Fisher Scientific) for dead cells for 2 minutes at room temperature. After rinsing with PBS, hydrogels were imaged using an epi-fluorescence microscope (Zeiss Axio Imager 2.0, Carl-Zeiss) with a 2.5 μm Z-stack over 150–200 μm sections.

2.8. Cell tracker and AlexaFluor staining

MCF-7 cells were labeled with cell tracker blue, red, or green (1 : 1000; Thermo Fisher Scientific) for 30 minutes before resuspension in 5% GelMA hydrogel (Porcine; Gelomics) for seeding. AlexaFluor 488, 555, or 647 dyes (1 : 250; Thermo Fisher Scientific) were added to GelMA, rat-tail collagen (PureCol), or PEG-Maleimide/thiolated-PEG hydrogels (JenKem Technologies) prior to seeding. Hydrogels were crosslinked using the LunaCrosslinker (Gelomics; GelMA), thermal gelation (collagen, 37 °C, pH 7, 40 minutes), or click chemistry (PEG). Images of hydrogel patterning were obtained *via* tile-imaging on a Zeiss Axio Imager 2.0.

2.9. Fluorescence imaging

Cell-laden gels were fixed *in situ* in the LM-Well with 4% paraformaldehyde (PFA) for 1 hour and stored in PBS at 4 °C. For staining, gels were blocked overnight at 4 °C in blocking buffer (5% goat serum (Thermo Fisher Scientific), 0.1% Triton X-100 (Sigma Aldrich) in PBS). For cytoskeletal visualization, gels were incubated with Alexa Fluor 488 Phalloidin (1 : 400; Thermo Fisher Scientific) in staining buffer (1% goat serum in PBS) overnight at 4 °C. C2C12 myosin heavy chain was stained with MyHC antibody (1 : 150; Thermo Fisher Scientific, 14-6503-82), and HIF1-α in MCF-7 and HepaRG cells was stained with HIF1-α antibody (1 : 150; Thermo Fisher Scientific, MA1-516), both overnight at 4 °C.

Secondary staining for MyHC and HIF1-α was performed with Alexa Fluor anti-mouse 488 secondary antibody (1 : 250; Thermo Fisher Scientific, A32766) overnight at 4 °C, alongside 5 μg mL^{-1} 4′,6-diamidino-2-phenylindole (DAPI; Thermo Fisher Scientific) for nuclear counterstaining. Samples were washed three times with staining buffer (2 hours each) and rinsed in PBS before storage. Imaging was performed using a confocal microscope (FV400, Olympus) with 10× and 20× objectives.

2.10. Myobundle construct width assessment

C2C12 cells were stained with DAPI and 488 phalloidin and imaged as described above, in addition to imaging with a Nikon Eclipse TS2 microscope. Then, myobundle construct width was measured using ImageJ.

2.11. RNA extraction, cDNA synthesis and quantitative polymerase chain reaction

Hydrogels were removed from the LM-Well by scooping with sterile spatulas and placed in Buffer RLT from the RNeasy Micro Kit (Qiagen) for RNA extraction following the manufacturer's protocol. Briefly, cells were lysed in Buffer RLT supplemented with β-mercaptoethanol (Sigma Aldrich), and the lysates were homogenized by passing through a QIAshredder column (Qiagen). Ethanol was added to the lysates to facilitate RNA binding, and the mixture was transferred to RNeasy spin columns. Columns were washed with buffers to remove contaminants, followed by RNA

elution in RNase-free water. RNA concentration and purity were assessed using a NanoDrop spectrophotometer (Thermo Fisher Scientific).

According to the manufacturer's protocol, cDNA was synthesized using the SensiFAST cDNA Synthesis Kit (Bioline). Briefly, 50 ng of total RNA was reverse-transcribed in a 20 μL reaction containing reverse transcription buffer, random primers, oligo (dT), and reverse transcriptase. The reaction was performed in a thermal cycler with the following conditions: 25 °C for 10 minutes, 42 °C for 15 minutes, and 85 °C for 5 minutes. The resulting cDNA was diluted 1 : 2 in nuclease-free water for subsequent qPCR.

Quantitative PCR (qPCR) was performed using the SensiFAST SYBR Lo-ROX Kit (Bioline) on a QuantStudio 6 Real-Time PCR System (Thermo Fisher Scientific). Reactions were conducted in 10 μL volumes, consisting of 5 μL of SensiFAST SYBR Lo-ROX Master Mix, 1 μL of cDNA, 3.2 μL of RNase-free water, and 0.4 μL of each primer (10 μM stock). The qPCR cycling conditions were as follows: an initial enzyme activation step at 95 °C for 2 minutes, followed by 40 cycles of 95 °C for 5 seconds and 60 °C for 30 seconds. A melt curve analysis was performed at the reaction's end to confirm the amplified products' specificity. Relative gene expression levels were determined using the $^{\Delta\Delta}$Ct method, with normalization to housekeeping genes. See supplementary materials for primer sequences (Table S1).

2.12. Oxygen-scavenging capsules seeding

Oxygen-scavenging capsules were sourced from collaborators whose work has been previously published.[44] In summary, oxygen-scavenging capsules coated with dopamine to imbue semi-permeable properties containing 1000 U mL^{-1} glucose oxidase and 60 000 U mL^{-1} catalase enzymes were provided at 500 mg mL^{-1} in 1× PBS. These capsules were then diluted according to the final concentrations in the hydrogels to between 2.5 and 7.5 mg mL^{-1} in the final hydrogels.

2.13. Oxygen measurements

Dissolved oxygen levels were measured *via* the PreSens OXY-1 ST trace (PreSens GmbH, #300000054) according to manufacturer's instructions, with the reading output recorded as equivalent oxygen saturation percentage in air ($\%O_2$). The probe was placed through the inlet hole to measure the oxygen tension in the hydrogel center (representative of the whole hydrogel), and six measurements were taken per sample.

2.14. HIF1-α quantification

Z-Stack images were condensed into a maximum intensity projection using ImageJ. Following this, a mask was created to capture the HIF1-α staining before the Mean Gray Value was collected as the intensity of the HIF1-α stain. Analysis was controlled for particle size (50 μm^2 to infinity) and circularity (0.3–1).

2.15. MCF-7 aggregate area assessment

Cells were stained with FDA and imaged as described in section 2.1.7. Resultant Z-stack images were condensed into a maximum intensity projection using ImageJ. Following this, a mask was created for the cells, upon which the 'analyze particles' feature was utilized to collect the area in μm^2 of each cellular aggregate. Analysis was controlled for particle size (75 μm^2 to infinity) and circularity (0.3–1).

2.16. Cytochrome P450 assay

As previously described, CYP3A4 activity was assessed using DBOMF dye (Thermo Fisher Scientific),[6] which is specifically cleaved by Cytochrome P450 3A4 (Cyp3A4) to produce a fluorescent product. On day 3 of HepaRG culture, 500 μL of differentiation media containing 2 μM dye replaced the existing media. Four hours later, the supernatant's fluorescence was measured at 490 nm excitation and 520 nm emission using a CLARIOstar Plus plate reader (BMG Labtech). Enzymatic activity was quantified from a standard curve in nM of dye cleaved per hour.

2.17. Drug studies

MCF-7 cells in GelMA hydrogels and HepaRG cells in liver click dECM hydrogels were seeded according to section 2.1.6. To facilitate co-culture, the MCF-7/GelMA hydrogels were first seeded into one leaflet of the LM-Well and crosslinked *via* visible light for 2 minutes. Following this, the HepaRG/click-dECM hydrogels were formed *via* click-chemistry in another well. Control wells contained only MCF-7 s and no HepaRG.

Tamoxifen (Merck Australia) was administered into the surrounding medium at a 100 μM final concentration for 48 hours with no media change, to allow the HepaRG to activate the drug. The media was then refreshed, and the cells underwent daily media changes for 3 days. On day 3, the MCF-7 cells were assessed for aggregate area using FDA staining and lysed for DNA quantitation.

Doxorubicin (Pfizer Australia Pty Ltd) was administered into the surrounding medium at a 400 nM final concentration for 24 hours before removing it, and the medium was refreshed. Cells then underwent daily media changes for 6 days. On day 6, the MCF-7 cells were assessed for aggregate area using FDA staining and lysed for DNA quantitation.

2.18. DNA quantitation

Cell-laden hydrogels were digested using RLT lysis buffer (QIAgen) and stored at −80 °C before DNA quantification with performed using the Quant-iT™ PicoGreen™ Kit (Thermo Fisher Scientific) was performed following manufacturer's instructions.

2.19. Statistical analysis

Statistical analysis was performed in GraphPad Prism v10. Unless otherwise noted, n = 3 technical replicates from n = 3 independent experiments are shown as mean ± SD.

Comparisons between two groups were conducted using Student's *t*-tests with Welch's correction, while comparisons between three or more groups used One-Way ANOVA with Tukey's multiple comparisons. Where equal standard deviation between groups was not present (identified by Bartlett's test), a Welch's ANOVA with Dunnett's T3 multiple comparisons was utilized. Outliers were excluded if identified by GraphPad's outlier analysis. Significance levels: $*p < 0.05$, $**p < 0.01$, $***p < 0.001$, $****p < 0.0001$.

3. Results

3.1. Design, fabrication and characterization of the 3D-printed LM-Well platform

The LM-Well was designed to be an open microfluidic device to facilitate the co-culture of three separate cell/hydrogel niches in a single 24-well (Fig. 1A). The device consisted of three scalloped flat leaflets suspended at a fixed height from the bottom of the well plate (Fig. 1A). This configuration created an open microfluidic channel, echoing previous works in open microfluidic patterning achieved by aspiration[39] and open microfluid well inserts,[40] that guided the hydrogel prepolymer solution *via* spontaneous capillary flow (SCF).[45] SCF occurs when the contact angle (θ) of the fluid interacting with the patterning structures (*i.e.* the leaflets and the well plate) is greater than the aspect ratio of the open microfluidic channel (eqn (1)[46,47]). This aspect ratio is defined as the gap height (h) between the leaflet and the base of the well plate, divided by the channel width (w). At the edge of the leaflets, the liquid flow is halted and the hydrogel is pinned in place due to the capillary burst effect, where a sudden expansion of the channel prevents further flow.[43]

$$\cos(\theta) > \frac{h}{w} \quad (1)$$

The scalloped-shaped leaflet was asymmetrically designed to maximize hydrogel occupancy within the well plate. Given this shape, the condition for SCF must be met at the smallest width (w) to facilitate hydrogel filling. Even if SCF can initiate upon entry into the channel (where the initial w is 10.89 mm; Fig. 1Aiv), it will not continue to fill the complete leaflet footprint once the aspect ratio fails to satisfy the condition for SCF. As such, we used the smallest width, the apex of the scallop shape at 1.5 mm (Fig. 1Aiv), to calculate the maximum allowable vertical gap (h) between the bottom of the leaflets and the base of the well plate. Based on a maximum contact angle (θ) of 58°, which was experimentally determined as the contact angle of water with FBS-coated 3D-printed plastic (data not shown), the optimal gap height was determined to be 0.8 mm to enable liquid patterning, provided that the contact angle remained below 58°. Most hydrogels meet this criterion, as their reported contact angles on similar surfaces fall well within this threshold. For example, Matrigel on plasma-treated FormLabs Clear resin has a contact angle of 22°,[40] collagen on glass is 24°,[48] and methacrylated hyaluronic acid hydrogel on glass and plastic is approximately 40°.[49] Hence, the LM-Well was designed to sit 0.8 mm above the base of the well, with its leaflets held in place by a central pillar.

3D printing was employed to generate these devices because it has been shown to be a powerful tool to rapidly generate complex geometries in microfluidic OoC devices.[36,50] However, many commercial biocompatible 3D printing resins were found to be cytotoxic in *in vitro* experiments.[51,52] Hence, we first evaluated the cytocompatibility of three commercially available 3D printing resins—TechClear (Moiin), BioMed Clear (FormLabs), and PlasClear (ASIGA) – with MCF-7 cells (Fig. S1A and B, SI Methods). 3D printed inserts at different stages of post-processing, *i.e.* before and after washing and over-curing were assessed. Both TechClear and BioMed Clear resins were biocompatible across all processing levels, while PlasClear exhibited cytotoxicity even after extensive post-processing (Fig. S1C). This aligns well with previous reports of toxicity with under and over-processed resins[36,53] and indicates the importance of such preliminary biocompatibility assessments. BioMed Clear resin was ultimately selected due to its cytocompatibility and higher throughput production capabilities with FormLabs printers.

Using the BioMed Clear resin, the final LM-Well insert design was 3D printed and assessed for print fidelity (Fig. 1B). The prints showed below 4% error compared to the CAD dimensions, indicating high reproducibility, for the height (A), leaflet length (B) and width (C), device inlet holes (D) and device internal (F) and external (G) width, with higher error (8%) for dimension E, which was designed to be the 1 mm gap between the leaflets (Fig. 1C). We then evaluated liquid patterning efficiency on uncoated (dry), wet and FBS-coated devices since the coating impacts the contact angle between the liquid and the leaflet. When the device was not coated, there was minimal patterning success, aligning with expectations as the cosine of the uncoated contact angle (θ = 78°) is less than the device's aspect ratio (Fig. 1D). Wetting the device in water before patterning did not enhance this, though soaking with FBS to impart a coating with adsorbed hydrophilic proteins on the device resulted in effective filling since the resultant contact angle (θ = 58°) was the smallest (Fig. 1D). Other hydrophilic protein coatings such as bovine serum albumin (BSA) are likely to similarly enhance filling. The volume of liquid patterned by each leaflet was reproducible, with the devices consistently patterning ~35 μL, ensuring a sufficient amount of cells and hydrogel for downstream biological assays (Fig. 1E).

We next sought to demonstrate the LM-Well's flexibility in patterning different classes of hydrogels. These included previously developed PEG-based click-chemistry hydrogels,[6] thermally crosslinked natural hydrogels (type I collagen), and photo-crosslinked GelMA (Fig. 1F). By suspending different cells, illustrated by cells labeled with different fluorescent probes, into the hydrogels, the LM-Well enabled the patterning of three distinct hydrogel niches with different cell populations (Fig. 1G). We verified the viability of cells encapsulated in a hydrogel patterned using the LM-Well compared to without the insert (Fig. 1H), confirming that the 3D-printed device has no adverse cytotoxic effects.

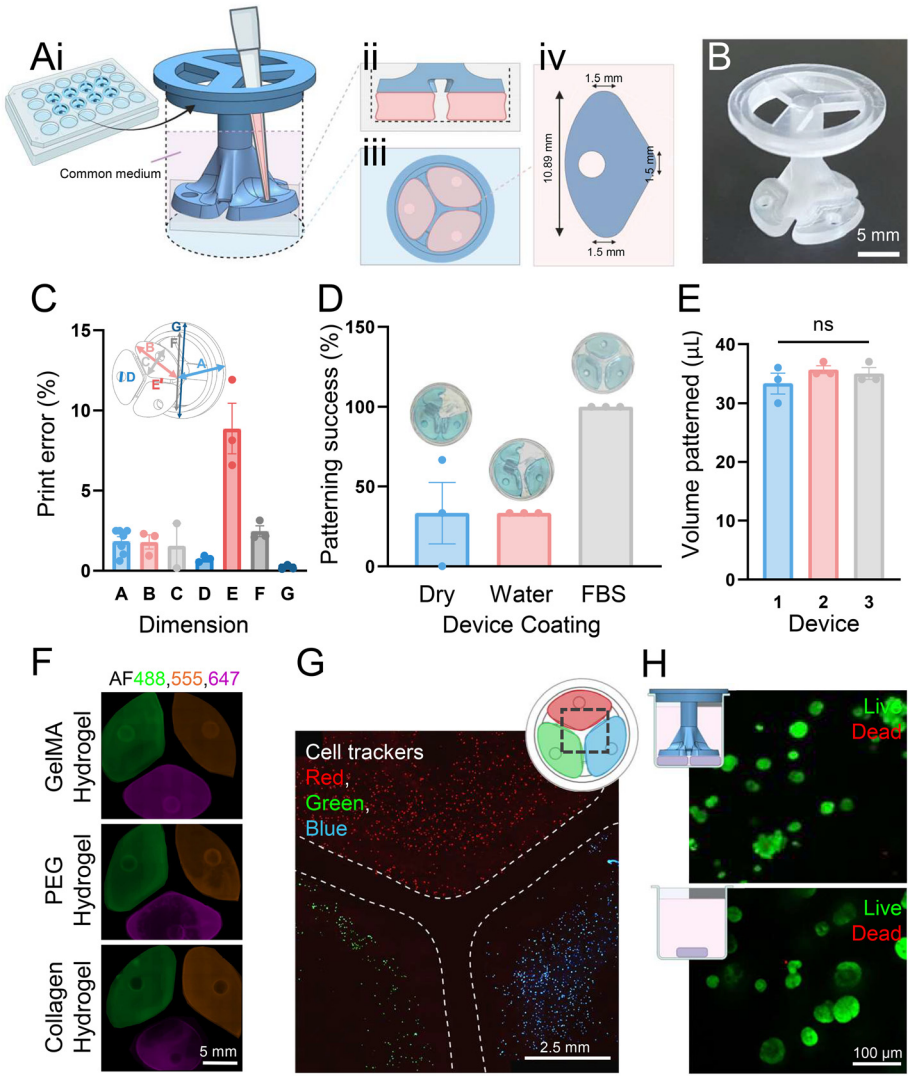

Fig. 1 LM-Well design and open microfluidic patterning characterization. (A) Schematic demonstrating the volume filling and patterning of hydrogels (pink) in a well of a 24-well plate by the LM-Well (blue). (i) Overall view of LM-Wells in a 24-well plate with close-up isometric view of an LM-Well in a 24-well plate well and indication of common medium, (ii) side-view of the hydrogel patterning between the bottom the LM-Well leaflets and the bottom of the well, (iii) bottom-view of the three distinct leaflets patterning hydrogels separately, (iv) indication of critical leaflet dimensions. (B) Pictograph of an LM-Well, scale bar represents 5 mm. (C) Print fidelity as print error (%), inlay shows relevant dimensions. (D) Accuracy of volume loading as success of localizing food-colored water with different coatings on the LM-Well, with representative bottom-view images. (E) Volume patterned under leaflet for three distinct devices. One-way ANOVA revealed no significant difference (ns) between devices. (F) Cell-free hydrogels with different Alexa Fluor (AF) tags patterned in the LM-Well, including GelMA hydrogel, PEG hydrogel (PEG-SH and PEG-MAL), and collagen 1 hydrogel. (G) MCF-7 cells in GelMA hydrogel tagged with different cell trackers patterned in the LM-Well. (H) Live/dead fluorescence imaging of MCF-7 cells in GelMA hydrogel with and without the LM-Well after 7 days of culture. All data is n = 3 devices with n = 3 technical replicates and mean ± SD.

3.2. Customizing niche physicochemical properties with oxygen-modulating microcapsules

Since the LM-Well utilizes open microfluidic patterning principles which are less dependent on hydrogel crosslinking properties, it allows one to incorporate additional functional materials to create patterned composite materials. The addition of oxygen-scavenging enzymes,[44] growth factors[54] or drugs[55,56] presents such opportunities for fine-tuning cellular microenvironments. Here, we demonstrate that previously developed oxygen-scavenging microcapsules[44] can be effectively patterned using the LM-Well, adding another layer of control over the physicochemical properties within this multi-niche system.

Local control of oxygen levels is crucial for replicating many physiological processes, as oxygen gradients exist in various tissues. For instance, hypoxic conditions are a hallmark of tumor microenvironments, such as those found in breast cancer.[57,58] At the same time, oxygen gradients are essential to mimic liver zonation of metabolic activities between the periportal and perivenous regions.[59–61] Although environmental chambers that regulate gas levels (*e.g.* hypoxic

incubators) can tune oxygen concentrations at a single set level,[44] they are limited in their ability to create stable, localized variations of oxygen levels as they impact the entire system.

To address this challenge, we incorporated microcapsules encapsulating glucose oxidase and catalase[44] into the hydrogels at varying concentrations before the LM-Well patterned them to produce multiple oxygen concentrations within a single well. The LM-Well's hydrogel patterning fidelity remained unaffected by the relatively large size and high concentration of the microcapsules, which typically increase material viscosity and could disrupt other patterning techniques, such as bioprinting.

We first demonstrate the use of the LM-Well to study hypoxic responses in breast cancer models within GelMA hydrogels, which are widely used in cancer research for their tunable properties.[62,63] After confirming that the effect of oxygen-scavenging microcapsules within one leaflet did not impact adjacent leaflets (Fig. S2), oxygen-scavenging capsules were incorporated at concentrations of 0, 5, and 7.5 mg mL^{-1} to establish localized regions of normoxia (~11% O_2) and varying degrees of hypoxia (8.9% and 6.5% O_2; Fig. 2A). MCF-7 breast cancer cells patterned within these localized oxygen environments responded correspondingly with increasing levels of Hypoxia-Inducible Factor 1 α (HIF1-α) at lower oxygen concentrations (Fig. 2B and C).[64] Indeed, single cells seeded within hypoxic regions formed smaller cellular aggregates (Fig. 2D and E), which was consistent with established literature on hypoxia-induced growth inhibition,[44,65] allowing us to capture distinct areas in hypoxic response in a single well.

Next, we moved to model metabolic liver zonation, where distinct oxygen regions within the liver correspond to defined metabolic activities. We employed HepaRG-derived hepatocytes in a liver click decellularized ECM (dECM) hydrogel previously developed by our group,[6] which provided a biologically relevant composition optimized for liver-specific cell functions. First, we utilized the same oxygen-scavenging capsule concentrations as with the MCF-7 cells, though, this resulted in extremely low oxygen levels (<3%) and cell death (data not shown). This could be due to the higher metabolic rate of hepatocytes as compared to cancer cells,[66] as well as the slightly higher seeding density used for the hepatocytes. As such, we reduced the concentrations of the oxygen-scavenging microcapsules to 2.5 and 5 mg mL^{-1} to achieve similar oxygen levels (8.7% and 5.2% O_2, respectively) to the hypoxic tumor models (Fig. 2F). Importantly, this matches the oxygen levels seen in different zones of the liver, where the periportal zone typically has an oxygen level of 8–9%, and the pericentral zone has an oxygen level of 4–5%.[67] Again, we observed a similar response in HIF1-α expression for HepaRG hepatocytes patterned within these localized oxygen environments (Fig. 2G and H). Excitingly, hepatocytes within these hypoxic niches exhibited decreased albumin expression and enhanced *CYP1A2* expression (Fig. 2I and J), replicating the zonation observed *in vivo*[61] without complex apparatus. Hence, by precisely patterning oxygen-scavenging capsules within these hydrogels, we generated localized oxygen gradients that mimic physiological conditions, demonstrating the platform's utility in creating highly controlled, model-specific microenvironments with targeted hydrogels and functional materials.

3.3. Integrating 3D printed micro-structures to customize local niches for mechanically active cells

Having shown the LM-Well to be well suited to generate niches comprising 3D cell-laden hydrogels, we moved to more complex niche formation involving providing scaffolding micro-structures for mechanically active cells, such as those of the mesenchymal lineage, including muscle or bone. These cells typically require matrix stiffnesses above what is usually achievable in hydrogels.[68] Hence, these mechanically active cells are ineffectively cultured when encapsulated within hydrogels and require scaffolds or pillars to act as anchor points.[69–74] Various 3D printing modalities suitable for fabricating more rigid biopolymers, such as fused deposition modeling (FDM) printing,[75] and melt electro-writing[76,77] have been used to manufacture 3D micro-structures for cell attachment. Hence, we harnessed the 3D-printed nature of the LM-Well to design additional 3D micro-structures, which can be printed directly on the base of the leaflets to support mechanically active cells.

We first assessed the print resolution limit of the 3D printer and found that struts above a 250 μm pillar diameter can be readily printed as part of the LM-Well leaflet with low error (Fig. 3A). With this limit identified, we printed two common 3D architectures used in tissue engineering – a cross-hatched scaffold (Fig. 3B) and a pair of hourglass shaped micro-pillars (Fig. 3C) often used in 3D myobundle formation.[78–80] In both designs, the dimensions of the struts were between 300 to 400 μm, with an inter-strut spacing of >700 μm, which are much larger than those obtained with PDMS replica molding (~20–100 μm;[73,74]) or melt electro-writing (10 μm;[76]). Nonetheless, C2C12 myoblast cells patterned using leaflets with the 3D cross-hatched scaffold exhibited a more spread cell morphology than those patterned in a collagen I hydrogel alone (Fig. 3D). This indicated that cells could respond to the differential mechanical environment imparted by adding rigid micro-structures.

Next, we demonstrate the generation of 3D myobundles to further illustrate the utility of the LM-Well with integrated 3D microstructures. The geometry of each leaflet was modified to pattern myoblast cells in collagen type 1 hydrogel into an elongated dog-bone-like structure, encapsulated two pairs of micropillars. Differentiation and remodeling of the myoblast cells around the micropillars as mechanical anchor points resulted in the formation of a 3D myobundle.[80,81] The first iteration of the elongated leaflet has a small width of 1 mm, disallowing effective SCF and, therefore, resulting in incomplete

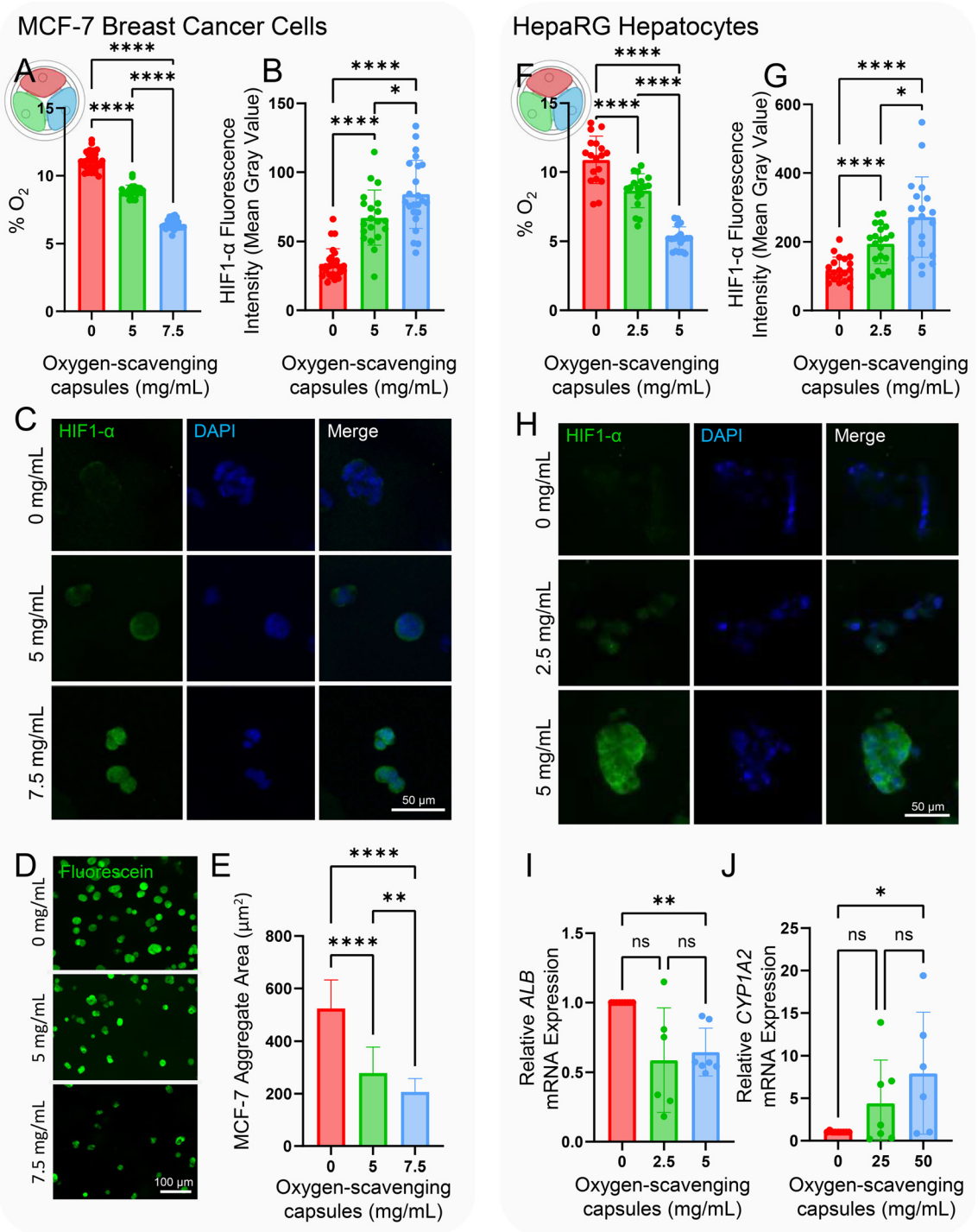

Fig. 2 Oxygen zonation in a single well using the LM-Well. Breast cancer zonation model (left) and HepaRG liver zonation model (right) shown. Percentage oxygen (A and F) and quantitative (B and G) and representative image HIF1-α expression (C,H) in three different leaflets which contain cells mixed with three different concentrations of oxygen-scavenging capsules (containing 1000 U mL^{-1} glucose oxidase and 60 000 U mL^{-1} catalase) on day 6 of MCF-7 culture (A–C) and day 3 of HepaRG culture (F–H). (D) Representative images of MCF-7 aggregate area patterning in a single well using different concentrations of oxygen-scavenging capsules, with quantification of aggregate area (E). (I and J) HepaRG liver zonation mRNA marker expression for a gene downregulated in hypoxia (ALB; I) and a gene upregulated in hypoxia (CYP1A2; J). All data is $n = 3$ experimental replicates of $n = 3$ devices each and mean ± SD. One-way ANOVA used for statistical analysis. ns = not significant, $*p < 0.05$, $**p < 0.01$, $***p < 0.001$, $****p < 0.0001$.

filling (Fig. 4A). However, when the width of the leaflet was expanded to 2.5 mm, we could achieve effective patterning around the pillars (Fig. 4A).

Using the successful second iteration of the pillar design, we analyzed the impact of pillar radius on myobundle construct formation (Fig. 4Bi). We found that constructs

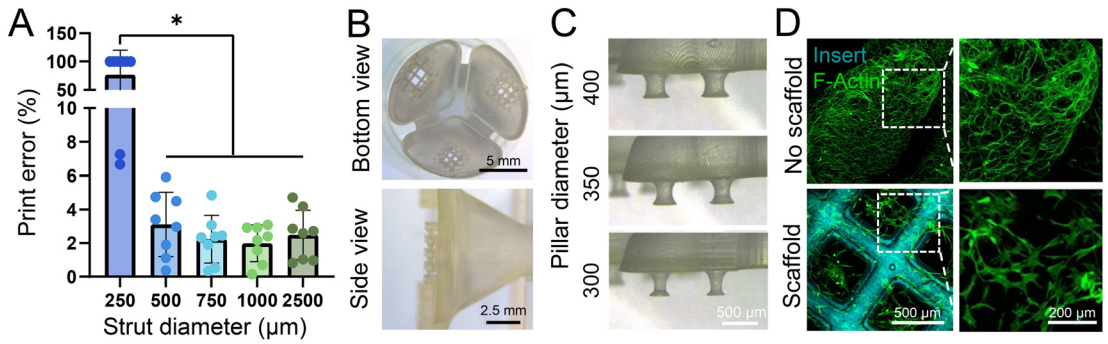

Fig. 3 Integration of micro-structures to the LM-Well. (A) Print error with different strut diameters, one-way ANOVA revealed significant (*$p < 0.05$) decrease in error above 250 μm strut radius. (B) Representative images of 3D printed cross-hatched scaffolds of 300 μm diameter at the base of the leaflets. (C) Representative images of hourglass-shaped pillars printed with different pillar diameters at the base of the leaflets. (D) Representative fluorescent images of C2C12 on day 9 of culture in collagen type I hydrogel with and without scaffold support.

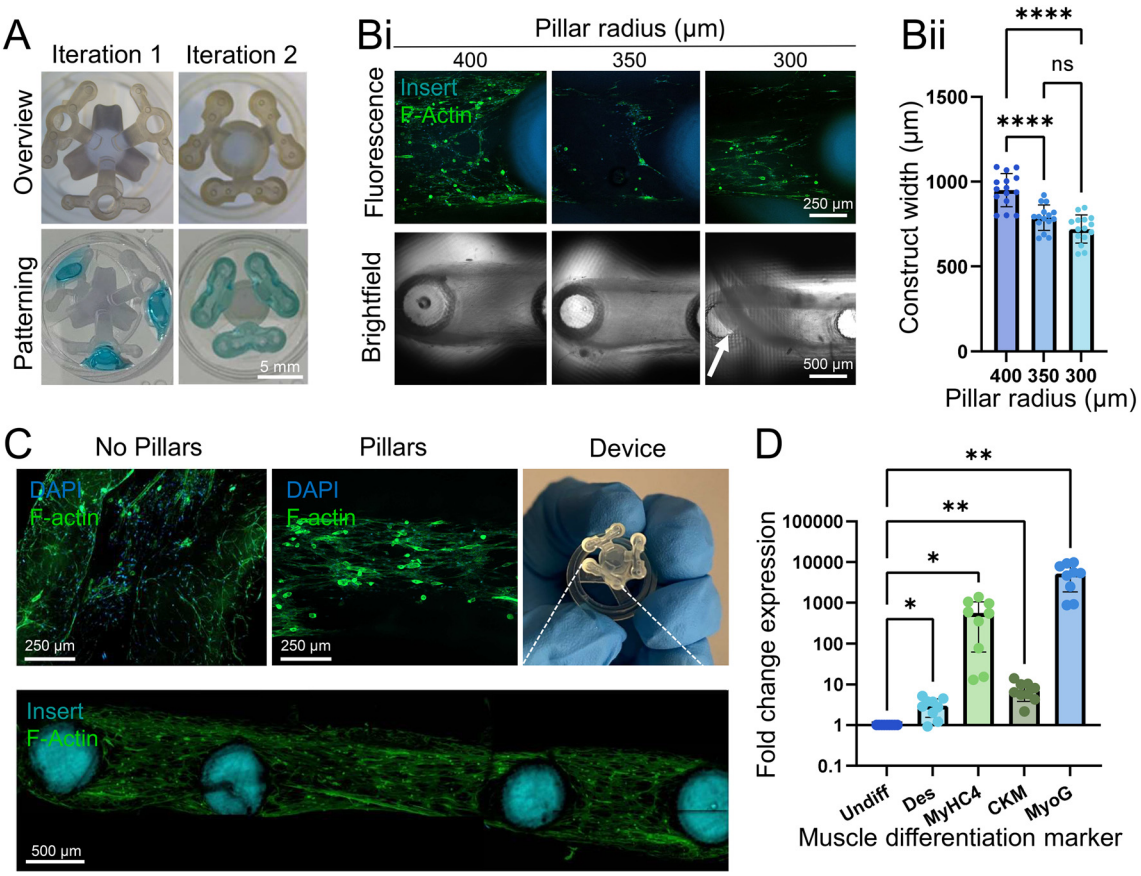

Fig. 4 Formation of C2C12 3D myobundles in a modified LM-Well with integrated micropillars. (A) Representative images of two iterations of the pillar-containing leaflets with food-colored liquid patterning to represent patterning ability. (B) (i) Fluorescence and brightfield imaging of C2C12/collagen type I constructs with (ii) C2C12 construct size. Arrow indicates construct lifted from the pillars. (C) Imaging of the C2C12 cells with and without the pillars after 9 days of culture, demonstration of retention of constructs upon removal from the well, and a tile image of the C2C12 construct. (D) mRNA expression of muscle differentiation markers on the LM-Well pillars compared to undifferentiated C2C12 cells on day 9 of culture. One-way ANOVA revealed significant upregulation, *$p < 0.05$, **$p < 0.01$.

could be formed between 0.8–1 mm in diameter (Fig. 4Bii) with all pillar radii tested. However, it was observed that pillars with a radius of 300 μm were unable to reliably support the cells, resulting in slippage of the myobundle (Fig. 4Bi). In contrast, pillars with radii of 350 μm and 400 μm supported the remodeling of C2C12/collagen into stable myobundle constructs (Fig. 4Bi). To minimize the risk of slippage and ensure robust myobundle stability, the 400 μm pillar diameter was selected for subsequent experiments.

We found the cells to align between the pillars when compared to a control with no pillars (Fig. 4C), and that the LM-Well design to allowed for convenient removal of the

device for confocal imaging, leveraging the autofluorescence of the device to visualize the pillars alongside the complete myobundle construct (Fig. 4C). Notably, the myobundles cultured on the modified LM-Well expressed muscle differentiation markers,[82,83] as confirmed by mRNA expression analysis, indicating successful differentiation of the muscle cells within the modified LM-Well (Fig. 4D). This result validates the LM-Well as a platform for culturing 3D myobundles with the modified muscle leaflet design, opening new possibilities for co-culturing myobundles alongside stromal or other supportive cells in adjacent leaflets, enabling the study of intercellular crosstalk. Additionally, the LM-Well facilitates the generation of myobundles in traditional well plates, providing a scalable and higher-throughput alternative to current PDMS-based systems.

3.4. Modelling liver-tumor crosstalk in a single well

Finally, we sought to demonstrate the LM-Well's utility in studying inter-organ crosstalk within a single well. In human physiology, multiple organs interact dynamically to produce coordinated functional outputs. This is especially important in the context of drug testing. Indeed, many pro-drugs rely on activation by the liver to achieve enhanced therapeutic activity following first-pass metabolism, which is crucial to capture in multi-tissue studies.[84,85] Tamoxifen is a well-known example, activated by hepatic enzymes into its more potent forms, 4-hydroxytamoxifen and endoxifen.[86] Neglecting liver functionality in such drug-testing models artificially diminishes the efficacy of tamoxifen, leading to inaccurate assessments. While complex and resource-intensive models involving manual assembly of laser-etched PDMS and acrylic pieces have previously demonstrated the necessity of liver activity for accurate tamoxifen studies,[87] we aimed to show that our simple, accessible LM-Well platform, which supports diverse biomaterial formulations, is similarly predictive and functional in this context.

The LM-Well was used to replicate key aspects of liver-tumor crosstalk while maintaining the functional integrity of both tissues. This system leverages hydrogels with two distinct crosslinking mechanisms to provide optimized microenvironments tailored to the specific needs of each cell type: photo-crosslinked GelMA for MCF-7 breast cancer cells,[25,88] and click-chemistry-based liver-dECM hydrogel for HepaRG-derived hepatocytes.[6]

The shared medium, essential for supporting both MCF-7 cells and HepaRG-hepatocytes and facilitating crosstalk, was optimized to maintain the viability and functionality of the respective cell types. MCF-7 cell viability was assessed *via* metabolic activity in three media formulations: MCF-7 medium, HepaRG medium, and a 1:1 mixture. HepaRG medium significantly reduced MCF-7 metabolic activity and aggregate size by day 7, whereas the 1:1 mixed medium maintained comparable aggregate size and metabolic activity to MCF-7 medium (Fig. S3A and B).

In addition to metabolic activity, HepaRG-hepatocyte metabolic functionality was further evaluated using cytochrome P450 3A4 (CYP3A4) activity as a key metric, as this enzyme metabolizes both tamoxifen and doxorubicin.[89,90] Surprisingly, HepaRG media was the least effective in supporting metabolic activity, while the 1:1 mixed medium enhanced both metabolic activity and CYPP3A4 activity by day 3, the critical time point for drug addition (Fig. S3C and D). Based on these results, the 1:1 mixed media was selected as the optimal formulation, supporting both MCF-7 viability and HepaRG-hepatocyte functionality for the subsequent drug study.

With an optimized co-culture medium, we studied liver-tumor crosstalk in drug metabolism and efficacy using the LM-Well platform. Drug concentrations were optimized with MCF-7 cells alone, with dose–response curves generated to determine a drug concentration corresponding to a 20–40% reduction in cell viability such that the drug efficacy can be modulated by the presence of HepaRG-hepatocytes (SI Fig. S4). We co-cultured the MCF-7 tumor cells and HepaRG-hepatocytes for 3 days before adding tamoxifen, and assessed the impact of pro-drug activation on MCF-7 cellular aggregates in conditions with and without the HepaRG-hepatocytes. By measuring DNA content as an indicator of MCF-7 cell growth, it was found that tamoxifen had no significant impact on the MCF-7 cells when cultured alone (Fig. 5A). However, in co-culture with the HepaRG-hepatocytes, there was a significant decrease in MCF-7 DNA amount, indicating that the activated tamoxifen stunted MCF-7 growth. This result concurred with observations in the aggregate size analysis (Fig. 5B and C), indicating that the drug was more effective in the presence of the HepaRG-hepatocytes.

We also investigated the effect of hepatic metabolism on doxorubicin clearance to demonstrate the importance of incorporating liver function when evaluating anti-tumor drug efficacy. Doxorubicin, a chemotherapy drug commonly used in breast cancer treatment, is metabolized by the liver into its less potent form, doxorubicinol, primarily through phase I enzymes such as CYP3A4 and CYP2B6, which are expressed in HepaRG-hepatocytes.[91] Therefore, we expect that when HepaRG-hepatocytes were co-cultured with MCF-7 cells in the LM-Well, the metabolic clearance of doxorubicin by the HepaRG-hepatocytes would reduce the anti-tumor efficacy of doxorubicin on MCF-7 cells. This was evidenced by increased total DNA content and cellular aggregate area in MCF-7 cultures compared to controls treated with doxorubicin without HepaRG-hepatocytes (Fig. 5D and F).

In addition to assessing MCF-7 tumor cells, we also examined the effects of tamoxifen and doxorubicin on HepaRG-hepatocytes within the LM-Well coculture. Both drugs markedly reduced the metabolic activity of HepaRG cells (SI Fig. S5), indicating hepatotoxic side effects consistent with previous reports in the literature.[92,93] To confirm that the observed differences in drug responses between tumor-only cultures and

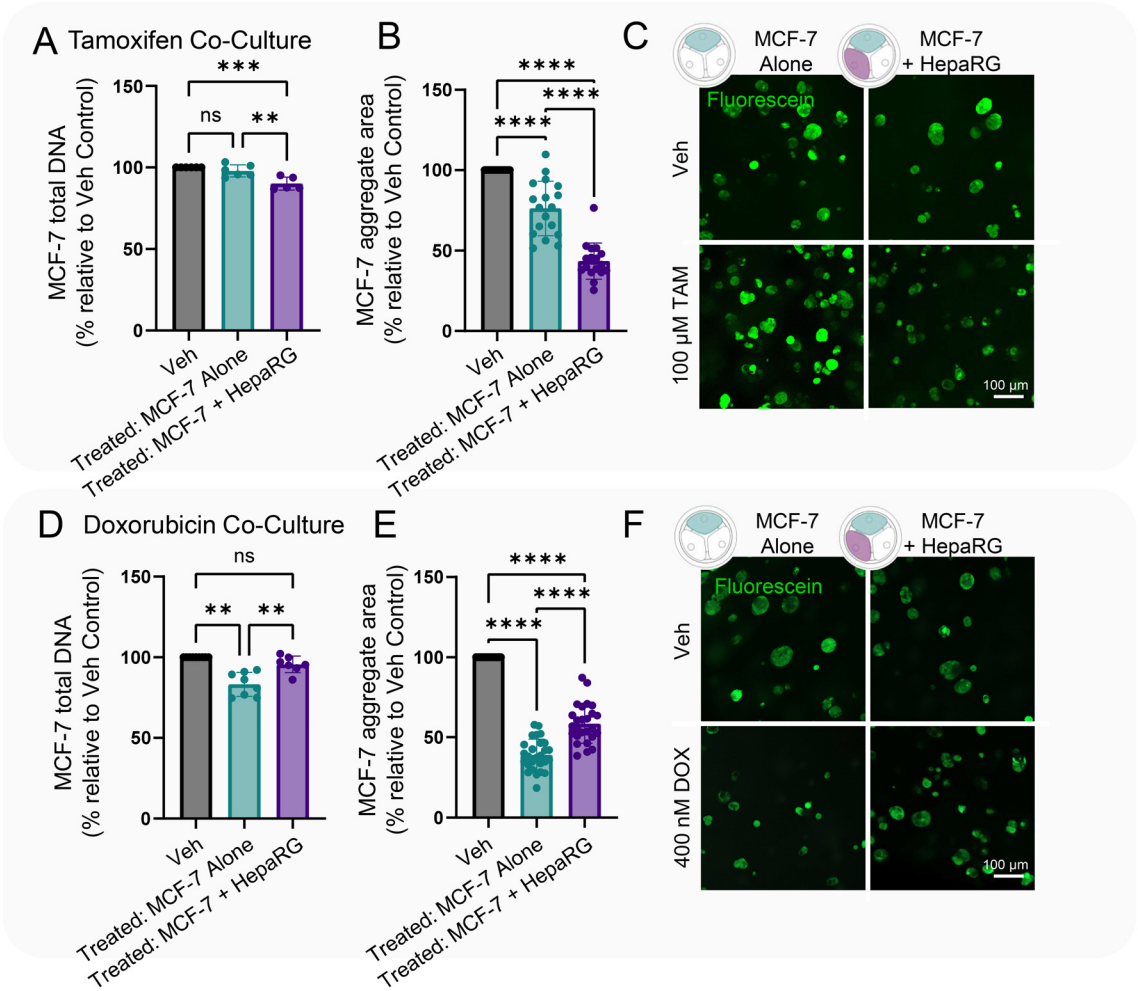

Fig. 5 Liver-tumor model tamoxifen (top) and doxorubicin (bottom) drug studies. MCF-7 total DNA (A) and aggregate area (B) as a percentage relative to the vehicle control, and representative aggregate images (C) for MCF-7 alone and MCF-7 + HepaRG conditions with 100 μM tamoxifen addition on day 3 of culture for 48 hours. MCF-7 total DNA (D) and aggregate area (E) as a percentage relative to the vehicle control, and representative aggregate images (F) for MCF-7 alone and MCF-7 + HepaRG conditions with 400 nM doxorubicin addition on day 6 of culture for 24 hours. All data is $n = 3$ experimental replicates of $n = 3$ devices each and mean ± SD. One-way ANOVA used for statistical analysis. ns = not significant, *$p < 0.05$, **$p < 0.01$, ***$p < 0.001$, ****$p < 0.0001$.

tumor–liver cocultures were specifically due to hepatic metabolic activity, rather than simply the presence of additional drug-sensitive cells, we performed a control experiment. In this setup, the HepaRG hepatic niche was replaced with a second MCF-7 tumor niche, thereby increasing the total number of tumor cells without introducing a metabolically active liver component. Under these conditions, no differential drug response to doxorubicin was observed (SI Fig. S6). These results demonstrate that while both tamoxifen and doxorubicin exhibit off-target hepatotoxicity, the presence of metabolically active HepaRG cells is essential to elicit the distinct drug response observed in the tumor–liver coculture.

The LM-Well thus successfully facilitated studies of crosstalk between two distinct cell types within a single well, with each cell type encapsulated in a tailored hydrogel with differing crosslinking mechanisms. Notably, this platform enabled the independent assessment of MCF-7 cells, even after co-culture with HepaRG cells, a feature not possible in direct co-culture setups and challenging in more complex systems.

4. Discussion

Studying multi-cellular interactions in an engineered physiological microenvironment is challenging. Significant complexity arises from the need to meet the specific environmental requirements of individual cell types while organizing them within a shared medium to facilitate effective communication.[1,2] Sizable efforts have been dedicated to developing advanced biomaterials that customize cellular microenvironments' biochemical and mechanical properties, enhancing their functionality and predictive value in disease modeling.[94,95] The LM-Well has been designed to provide an accessible and easy-to-use platform for patterning such various hydrogels, regardless of their material properties. This 3D-printed open microfluidic

well insert utilizes SCF to pattern cell-containing prepolymer solutions into distinct regions within a single well. This capability enables the creation of various niches defined by hydrogel composition, additional biomaterials, structural supports, and the cell types present. All these elements contribute to forming a complex localized microenvironment with unique characteristics.

Fluid patterning by the LM-Well relies on capillary force-driven SCF, which is governed by the wettability of the polymer solution on the 3D-printed resin and the aspect ratio of the open microfluidic channel,[46,47] determined by the leaflet width and the gap height between the leaflet and the well plate. Since SCF is independent of bulk material properties, such as viscosity or other rheological characteristics, any Newtonian fluid can be successfully patterned. Viscosity does not play a role in the conditions for successful flow, but does slow the flow dynamics, potentially increasing the time taken to pattern materials.[96] The versatility of the LM-Well was demonstrated through our successful integration of diverse biomaterials, including rat-tail collagen for C2C12 myobundle formation, GelMA for MCF-7 breast cancer cells, and liver-dECM gels for HepaRG-hepatocytes, and we anticipate that the LM-Well would be amenable for use with a vast library of biomaterials that is ever expanding.[97]

The LM-Well also allows for configurable hydrogel geometry and spatial patterning. In this study, it was designed to create three independent niches within a 24-well plate. Leaflets of different shapes can be tailored for cell-type-specific co-culture within a single well, provided that SCF conditions are met. We demonstrated this versatility by modifying the leaflet shape from three evenly distributed, scallop-shaped sections circumscribed by the 24-well to an elongated dog-bone format for myobundle culture. Further, well inserts for different plate formats including 6, 12, 48 and 96-well plates could be designed. In larger well plat formats (*e.g.* 6-well), more than three patterning leaflets could be designed to generate more than three cell niches for extensive multi-organ studies. Moreover, it could allow for higher throughput experiments with smaller footprint well plates. SCF conditions can likely be satisfied by reducing the gap height between the bottom of the leaflet and the base of the well when the leaflet area decreases. The diffusion distance between leaflets is another critical factor in scaling down the LM-Well. We found the adjacent leaflets in our model to have little impact on one another, best demonstrated by the distinct patterning of oxygen scavengers in the LM-Well (Fig. S2). The oxygen-scavenging microcapsules have a diffusive range of approximately 3 mm.[44] This allowed for precise control in our relatively large leaflets but could impact distinct niche formation in smaller footprints. However, if the conditions for SCF are satisfied and the space between leaflets is sufficient to allow for distinct patterning, many different embodiments of the LM-Well are possible.

Further adaptability could be imbued to the LM-Well by incorporating functional materials, such as nano- or micro-particles, or the addition of 3D printed structures to the bottom of the leaflets. Here, we demonstrated the incorporation of oxygen-scavenging micro-capsules to control the local oxygen level within a cell niche. Other functional materials, such as smart polymers or nanoparticles that control the delivery of growth factors[54] or drugs[55,56] could also be incorporated. An exciting opportunity could be the integration of sensor materials, such as oxygen biosensors along with oxygen-scavenging micro-capsules to allow concurrent measurement of local oxygen levels along with the oxygen patterning.[98] Moreover, with the advent of 3D printing technologies, there are opportunities to add higher resolution structures to the base of the LM-Well. This could allow for embodiments of the LM-Well with precise 3D printed scaffolds for osteosarcoma modelling,[99] or scaffolds with gradient structures to mimic physiology in bone regeneration.[100] Moreover, using multi-material printers could allow for incorporating electrophysiological recording or stimulation with gold pillars embedded in the hydrogels[101] or flexible pillars for quantifying contractile functions using inverted microscopy.[102] As there continues to be advances in 3D printing resolution and complexity, this can be translated to niche complexity in the LM-Well.

The LM-Well bridges the gap between experimental complexity and analytical accessibility. The open-well format and removability of the LM-Well following experimentation facilitated the harvesting of hydrogel for downstream analyses, such as imaging, gene expression profiling, and biochemical assays. Hydrogels from separate leaflets could be scooped from the well and analyzed individually. In contrast, traditional microfluidic setups often isolate cells in enclosed microfluidic channels, making them difficult to harvest.[103] This feature was particularly valuable in our research for harvesting cells subjected to separate hypoxic niches to examine their phenotype and functions. When examining multicellular crosstalk, such as the effect of liver metabolism on tamoxifen and doxorubicin efficacy on MCF-7 breast cancer cells, the LM-Well allowed crosstalk between the liver and tumor niches in shared media but enabled MCF-7 tumor cells to be harvested in isolation from the LM-Well specifically for analyses. While the study of tamoxifen activation by liver cells is not novel, with previous OoC studies demonstrating the role of the liver in tamoxifen activation,[87] existing models often rely on complex apparatus, such as perfusion systems, and require disassembly of the device to retrieve cells cultured on coverslips.[87] These processes can be labor-intensive and introduce variability. In contrast, the LM-Well achieved similar results with additional readouts, including aggregate size and DNA content, in a more straightforward setup that is amenable to standard laboratory environments. This was also found in our study on doxorubicin metabolism where we identified results that aligned with established literature in far more complex settings.[104,105]

The LM-Well is designed to pattern cell-laden hydrogels within a shared soluble microenvironment in a well plate. While this simplified operation, it also poses challenges, particularly for co-culturing multiple cell types, as

maintaining a common medium that is optimal for all cell types can be difficult, especially if fastidious cells like primary or stem cells are involved. A simple workaround solution would be mixing different media in specific ratios[106] as we have shown in the liver-tumor co-culture study. This solution may not always be applicable, especially when some factors present in one cell type's media may inhibit another cell type's function, as was the case in a multi-organ model where TGF-β1 was found to be required for lung cell function but inhibit liver function.[107] As an alternative, universal mediums are being developed to support the culture of multiple cell types,[108] though these remain primarily in development.

Regarding modeling multi-cellular crosstalk, the LM-Well is best suited for modeling interactions driven by paracrine signaling, particularly those between parenchymal and stromal tissues within or across organ systems. Within an organ system, the LM-Well can be used to study microenvironmental heterogeneity such as oxygen levels in liver zonation and drug efficacy within solid tumors. Between organ systems, we anticipate it to be suitable for investigating metabolic organ crosstalk including that between adipose, liver and muscle tissue,[109] or immunity with cancer-associated fibroblasts producing factors that may alter tumorigenicity or the drug responses of tumor cells.[110] Beyond fundamental studies of cellular crosstalk, the LM-Well could also be applied to pharmaceutical contexts, including potential higher-throughput screenings of drug–drug interactions or assessing metabolite-mediated toxicity. Careful adaptation would be needed, particularly to integrate with automation workflows common in the pharmaceutical industry. While powerful for multiple applications, the LM-Well is less suited for migration studies like tumor metastasis from the solid tumor into the vasculature which require direct cell–cell contact or translocation across barrier tissues. Also, pharmacodynamics/pharmacokinetics studies involving more than three or four cell types may be complex due to the practicality of patterning many tissues in a single well, and the lack of dynamic flow to control the relative distribution of drugs, simulating systemic blood flow to different organ systems.[111]

Conclusion

The LM-Well provides a versatile and accessible platform for spatially organizing biomaterials and creating localized microenvironments within traditional well plates. It supports a wide range of biomaterials, allows for precise control over microenvironmental conditions, and facilitates downstream analyses. These features make the LM-Well a robust tool for researchers investigating tissue-specific microenvironments, cellular interactions, and drug metabolism. Its simplicity and adaptability make the LM-Well a valuable resource for enhancing our understanding of complex biological systems.

Author contributions

Laura A. Milton: writing – original draft, visualization, methodology, investigation, formal analysis, data curation, conceptualization. Surasak Kasetsirikul: data curation. Jorge A. Catano: visualization, methodology. F. Sofia Hilmi: methodology, data curation. Zeheng Zhou: methodology, resources. Thomas G. Molley: methodology, resources. Kristopher Kilian: methodology, resources. Louis J. Y. Ong: methodology, data curation. James Chirnside: data curation. Nicholas Byrom: data curation. Georgia Balshaw: data curation. Sammy Liang: data curation. Laura J. Bray: methodology, resources. Dietmar W. Hutmacher: writing – review and editing, supervision. Christoph Meinert: writing – review and editing, supervision. Yi-Chin Toh: writing – review and editing, supervision, methodology, conceptualization.

Conflicts of interest

The authors declare the following financial interests/personal relationships which may be considered as potential competing interests: Christoph Meinert reports a relationship with Gelomics Pty Ltd. that includes: board membership, employment, and equity or stocks. Dietmar W. Hutmacher reports a relationship with Gelomics Pty Ltd. that includes: equity or stocks. Thomas G. Molley reports a relationship with OxyLo Inc. that includes: board membership, employment, and equity or stocks. Kristopher A. Kilian reports a relationship with OxyLo Inc. that includes: equity or stocks. If there are other authors, they declare that they have no known competing financial interests or personal relationships that could have appeared to influence the work reported in this paper.

Data availability

Supplementary information is available. See DOI: **https://doi.org/10.1039/D5LC00753D**.

Data for this article, including CAD files for all well inserts are available at Open Science Framework (OSF) at **https://doi.org/10.17605/OSF.IO/NZWXP**.

Acknowledgements

This work was supported by the Australian Research Council (FT180100157, DP200101658, DP230100721) awarded to YCT; Cooperative Research Centres Projects (CRCPXIV000130) awarded to CM and YCT. FSH, LJB and YCT acknowledge the Australian Research Council for funding of an Industrial Transformation Training Centre in Cell and Tissue Engineering Technologies (IC190100026). LM is supported by QUT Postgraduate Research Award (QUTPRA) and QUT Centre for Biomedical Technologies top-up scholarship. This work was enabled using the Central Analytical Research Facility (CARF) at the Queensland University of Technology (QUT).

References

1 N. Picollet-D'hahan, A. Zuchowska, I. Lemeunier and S. Le Gac, Multiorgan-on-a-Chip: A Systemic Approach To Model and Decipher Inter-Organ Communication, *Trends Biotechnol.*, 2021, **39**(8), 788–810.

2 Y. Zhao, R. K. Kankala, S. B. Wang and A. Z. Chen, Multi-Organs-on-Chips: Towards Long-Term Biomedical Investigations, *Molecules*, 2019, **24**(4), 675.

3 S. Maji and H. Lee, Engineering Hydrogels for the Development of Three-Dimensional In Vitro Models, *Int. J. Mol. Sci.*, 2022, **23**(5), 2662.

4 S. L. Vega, M. Y. Kwon and J. A. Burdick, Recent advances in hydrogels for cartilage tissue engineering, *Eur. Cells Mater.*, 2017, **33**, 59–75.

5 T. C. Ho, C. C. Chang, H. P. Chan, T. W. Chung, C. W. Shu, K. P. Chuang, T. H. Duh, M. H. Yang and Y. C. Tyan, Hydrogels: Properties and Applications in Biomedicine, *Molecules*, 2022, **27**(9), 2902.

6 L. A. Milton, J. W. Davern, L. Hipwood, J. C. S. Chaves, J. McGovern, D. Broszczak, D. W. Hutmacher, C. Meinert and Y.-C. Toh, Liver click dECM hydrogels for engineering hepatic microenvironments, *Acta Biomater.*, 2024, **185**, 144–160.

7 X. Ma, C. Yu, P. Wang, W. Xu, X. Wan, C. S. E. Lai, J. Liu, A. Koroleva-Maharajh and S. Chen, Rapid 3D bioprinting of decellularized extracellular matrix with regionally varied mechanical properties and biomimetic microarchitecture, *Biomaterials*, 2018, **185**, 310–321.

8 L. J. Bray, M. Binner, A. Holzheu, J. Friedrichs, U. Freudenberg, D. W. Hutmacher and C. Werner, Multi-parametric hydrogels support 3D in vitro bioengineered microenvironment models of tumour angiogenesis, *Biomaterials*, 2015, **53**, 609–620.

9 L. M. Caballero Aguilar, A. Trengove, S. M. Silva, A. Xie, C. O'Connell, C. Di Bella, S. Duchi, C. Onofrillo and S. E. Moulton, Electrostatic complexation of growth factors in thiol-armed hydrogel enhances in situ cartilage tissue engineering, *Appl. Mater. Today*, 2024, **38**, 102181.

10 D. Lu, K. Cai, Z. Zeng, J. Huang, N. Ma, B. Gao and S. Yu, VEGF loading heparinized hyaluronic acid macroporous hydrogels for enhanced 3D endothelial cell migration and vascularization, *Biomater. Adv.*, 2025, **167**, 214094.

11 S. Santoni, S. G. Gugliandolo, M. Sponchioni, D. Moscatelli and B. M. Colosimo, 3D bioprinting: current status and trends—a guide to the literature and industrial practice, *Bio-Des. Manuf.*, 2022, **5**(1), 14–42.

12 S. Liu, L. Cheng, Y. Liu, H. Zhang, Y. Song, J. H. Park, K. Dashnyam, J. H. Lee, F. A. Khalak, O. Riester, Z. Shi, S. Ostrovidov, H. Kaji, H. P. Deigner, J. L. Pedraz, J. C. Knowles, Q. Hu, H. W. Kim and M. Ramalingam, 3D Bioprinting tissue analogs: Current development and translational implications, *J. Tissue Eng.*, 2023, **14**, 20417314231187113.

13 P. Bramhe, N. Rarokar, R. Kumbhalkar, S. Saoji and P. Khedekar, Natural and synthetic polymeric hydrogel: A bioink for 3D bioprinting of tissue models, *J. Drug Delivery Sci. Technol.*, 2024, **101**, 106204.

14 H. H. Hwang, S. You, X. Ma, L. Kwe, G. Victorine, N. Lawrence, X. Wan, H. Shen, W. Zhu and S. Chen, High throughput direct 3D bioprinting in multiwell plates, *Biofabrication*, 2021, **13**(2), 025007.

15 M. Jung, J. N. Skhinas, E. Y. Du, M. A. K. Tolentino, R. H. Utama, M. Engel, A. Volkerling, A. Sexton, A. P. O'Mahony, J. C. C. Ribeiro, J. J. Gooding and M. Kavallaris, A high-throughput 3D bioprinted cancer cell migration and invasion model with versatile and broad biological applicability, *Biomater. Sci.*, 2022, **10**(20), 5876–5887.

16 A. C. Dell, G. Wagner, J. Own and J. P. Geibel, 3D Bioprinting Using Hydrogels: Cell Inks and Tissue Engineering Applications, *Pharmaceutics*, 2022, **14**(12), 2596.

17 P. S. Gungor-Ozkerim, I. Inci, Y. S. Zhang, A. Khademhosseini and M. R. Dokmeci, Bioinks for 3D bioprinting: an overview, *Biomater. Sci.*, 2018, **6**(5), 915–946.

18 N. E. Vrana, S. Gupta, K. Mitra, A. A. Rizvanov, V. V. Solovyeva, E. Antmen, M. Salehi, A. Ehterami, L. Pourchet, J. Barthes, C. A. Marquette, M. von Unge, C.-Y. Wang, P.-L. Lai and A. Bit, From 3D printing to 3D bioprinting: the material properties of polymeric material and its derived bioink for achieving tissue specific architectures, *Cell Tissue Banking*, 2022, **23**(3), 417–440.

19 W. Fang, M. Yang, L. Wang, W. Li, M. Liu, Y. Jin, Y. Wang, R. Yang, Y. Wang, K. Zhang and Q. Fu, Hydrogels for 3D bioprinting in tissue engineering and regenerative medicine: Current progress and challenges, *IJB*, 2023, **9**(5), 759.

20 B. E. Grottkau, Z. Hui and Y. Pang, A Novel 3D Bioprinter Using Direct-Volumetric Drop-On-Demand Technology for Fabricating Micro-Tissues and Drug-Delivery, *Int. J. Mol. Sci.*, 2020, **21**(10), 3482.

21 J. Weygant, F. Koch, K. Adam, K. Tröndle, R. Zengerle, G. Finkenzeller, S. Kartmann, P. Koltay and S. Zimmermann, A Drop-on-Demand Bioprinting Approach to Spatially Arrange Multiple Cell Types and Monitor Their Cell-Cell Interactions towards Vascularization Based on Endothelial Cells and Mesenchymal Stem Cells, *Cell*, 2023, **12**(4), 646.

22 X. Lan, A. Adesida and Y. Boluk, Rheological and viscoelastic properties of collagens and their role in bioprinting by micro-extrusion, *Biomed. Mater.*, 2022, **17**(6), 062005.

23 J. Yang, H. He, D. Li, Q. Zhang, L. Xu and C. Ruan, Advanced strategies in the application of gelatin-based bioink for extrusion bioprinting, *Bio-Des. Manuf.*, 2023, **6**(5), 586–608.

24 B. J. Gill and J. L. West, Modeling the tumor extracellular matrix: Tissue engineering tools repurposed towards new frontiers in cancer biology, *J. Biomech.*, 2014, **47**(9), 1969–1978.

25 N. Bock, F. Forouz, L. Hipwood, J. Clegg, P. Jeffery, M. Gough, T. van Wyngaard, C. Pyke, M. N. Adams, L. J. Bray, L. Croft, E. W. Thompson, T. Kryza and C. Meinert, GelMA, Click-Chemistry Gelatin and Bioprinted Polyethylene Glycol-Based Hydrogels as 3D Ex Vivo Drug Testing

Platforms for Patient-Derived Breast Cancer Organoids, *Pharmaceutics*, 2023, **15**(1), 261.
26 F. Tabatabaei, K. Moharamzadeh and L. Tayebi, Fibroblast encapsulation in gelatin methacryloyl (GelMA) versus collagen hydrogel as substrates for oral mucosa tissue engineering, *J. Oral Biol. Craniofac. Res.*, 2020, **10**(4), 573–577.
27 Y. Liu, Z. Li, J. Li, S. Yang, Y. Zhang, B. Yao, W. Song, X. Fu and S. Huang, Stiffness-mediated mesenchymal stem cell fate decision in 3D-bioprinted hydrogels, Burns, *Trauma*, 2020, **8**, tkaa029.
28 A. Urciuolo, E. Serena, R. Ghua, S. Zatti, M. Giomo, N. Mattei, M. Vetralla, G. Selmin, C. Luni, N. Vitulo, G. Valle, L. Vitiello and N. Elvassore, Engineering a 3D in vitro model of human skeletal muscle at the single fiber scale, *PLoS One*, 2020, **15**(5), e0232081.
29 Z. Wan, A. X. Zhong, S. Zhang, G. Pavlou, M. F. Coughlin, S. E. Shelton, H. T. Nguyen, J. H. Lorch, D. A. Barbie and R. D. Kamm, A Robust Method for Perfusable Microvascular Network Formation In Vitro, *Small Methods*, 2022, **6**(6), e2200143.
30 P. Vulto, S. Podszun, P. Meyer, C. Hermann, A. Manz and G. A. Urban, Phaseguides: a paradigm shift in microfluidic priming and emptying, *Lab Chip*, 2011, **11**(9), 1596–1602.
31 C. Su, Y. J. Chuah, H. B. Ong, H. M. Tay, R. Dalan and H. W. Hou, A Facile and Scalable Hydrogel Patterning Method for Microfluidic 3D Cell Culture and Spheroid-in-Gel Culture Array, *Biosensors*, 2021, 509.
32 C. M. Leung, P. de Haan, K. Ronaldson-Bouchard, G.-A. Kim, J. Ko, H. S. Rho, Z. Chen, P. Habibovic, N. L. Jeon, S. Takayama, M. L. Shuler, G. Vunjak-Novakovic, O. Frey, E. Verpoorte and Y.-C. Toh, A guide to the organ-on-a-chip, *Nat. Rev. Methods Primers*, 2022, **2**(1), 33.
33 H. T. Nguyen, E. L. Kan, M. Humayun, N. Gurvich, G. S. Offeddu, Z. Wan, M. F. Coughlin, D. C. Renteria, A. Loew, S. Wilson, C. Zhang, V. Vu, S. W. L. Lee, S.-L. Tan, D. Barbie, J. Hsu, M. R. Gillrie and R. D. Kamm, Patient-specific vascularized tumor model: Blocking monocyte recruitment with multispecific antibodies targeting CCR2 and CSF-1R, *Biomaterials*, 2025, **312**, 122731.
34 O. Jung, Y. T. Tung, E. Sim, Y. C. Chen, E. Lee, M. Ferrer and M. J. Song, Development of human-derived, three-dimensional respiratory epithelial tissue constructs with perfusable microvasculature on a high-throughput microfluidics screening platform, *Biofabrication*, 2022, **14**(2), 025012.
35 A. Skardal, S. V. Murphy, M. Devarasetty, I. Mead, H. W. Kang, Y. J. Seol, Y. Shrike Zhang, S. R. Shin, L. Zhao, J. Aleman, A. R. Hall, T. D. Shupe, A. Kleensang, M. R. Dokmeci, S. Jin Lee, J. D. Jackson, J. J. Yoo, T. Hartung, A. Khademhosseini, S. Soker, C. E. Bishop and A. Atala, Multi-tissue interactions in an integrated three-tissue organ-on-a-chip platform, *Sci. Rep.*, 2017, **7**(1), 8837.
36 L. A. Milton, M. S. Viglione, L. J. Y. Ong, G. P. Nordin and Y.-C. Toh, Vat photopolymerization 3D printed microfluidic devices for organ-on-a-chip applications, *Lab Chip*, 2023, **23**(16), 3537–3560.
37 J. Berthier, A. B. Theberge and E. Berthier, *Open-Channel Microfluidics, Fundamentals and applications*, IOP Publishing, 2nd edn, 2024.
38 S. Jung, S. Cheong, Y. Lee, J. Lee, J. Lee, M. S. Kwon, Y. S. Oh, T. Kim, S. Ha, S. J. Kim, D. H. Jo, J. Ko and N. L. Jeon, Integrating Vascular Phenotypic and Proteomic Analysis in an Open Microfluidic Platform, *ACS Nano*, 2024, **18**(36), 24909–24928.
39 D. Park, J. Lee, Y. Lee, K. Son, J. W. Choi, W. J. Jeang, H. Choi, Y. Hwang, H.-Y. Kim and N. L. Jeon, Aspiration-mediated hydrogel micropatterning using rail-based open microfluidic devices for high-throughput 3D cell culture, *Sci. Rep.*, 2021, **11**(1), 19986.
40 S. B. Berry, T. Zhang, J. H. Day, X. Su, I. Z. Wilson, E. Berthier and A. B. Theberge, Upgrading well plates using open microfluidic patterning, *Lab Chip*, 2017, **17**(24), 4253–4264.
41 J. H. Day, T. M. Nicholson, X. Su, T. L. van Neel, I. Clinton, A. Kothandapani, J. Lee, M. H. Greenberg, J. K. Amory, T. J. Walsh, C. H. Muller, O. E. Franco, C. R. Jefcoate, S. E. Crawford, J. S. Jorgensen and A. B. Theberge, Injection molded open microfluidic well plate inserts for user-friendly coculture and microscopy, *Lab Chip*, 2020, **20**(1), 107–119.
42 V. Mehta and S. N. Rath, 3D printed microfluidic devices: a review focused on four fundamental manufacturing approaches and implications on the field of healthcare, *Bio-Des. Manuf.*, 2021, **4**(2), 311–343.
43 H. Cho, H.-Y. Kim, J. Y. Kang and T. S. Kim, How the capillary burst microvalve works, *J. Colloid Interface Sci.*, 2007, **306**(2), 379–385.
44 T. G. Molley, S. Jiang, L. Ong, C. Kopecky, C. D. Ranaweera, G. K. Jalandhra, L. Milton, E. Kardia, Z. Zhou, J. Rnjak-Kovacina, S. A. Waters, Y. C. Toh and K. A. Kilian, Gas-modulating microcapsules for spatiotemporal control of hypoxia, *Proc. Natl. Acad. Sci. U. S. A.*, 2023, **120**(16), e2217557120.
45 J. Berthier, K. A. Brakke and E. Berthier, A general condition for spontaneous capillary flow in uniform cross-section microchannels, *Microfluid. Nanofluid.*, 2014, **16**(4), 779–785.
46 B. P. Casavant, E. Berthier, A. B. Theberge, J. Berthier, S. I. Montanez-Sauri, L. L. Bischel, K. A. Brakke, C. J. Hedman, W. Bushman, N. P. Keller and D. J. Beebe, Suspended microfluidics, *Proc. Natl. Acad. Sci. U. S. A.*, 2013, **110**, 10111–10116.
47 E. Berthier, A. M. Dostie, U. N. Lee, J. Berthier and A. B. Theberge, Open Microfluidic Capillary Systems, *Anal. Chem.*, 2019, **91**(14), 8739–8750.
48 M. Amer, F. Rose, K. Shakesheff and L. White, A biomaterials approach to influence stem cell fate in injectable cell-based therapies, *Stem Cell Res. Ther.*, 2018, **9**, 39.
49 F. Chen, S. Gu, Q. Zhang, T. Liu, Z. Liu and T. Kuang, A comparison study of hyaluronic acid hydrogel exquisite micropatterns with photolithography and light-cured inkjet printing methods, *e-Polymers*, 2022, **22**, 332–341.

50 V. Carvalho, I. Gonçalves, T. Lage, R. O. Rodrigues, G. Minas, S. Teixeira, A. S. Moita, T. Hori, H. Kaji and R. A. Lima, 3D Printing Techniques and Their Applications to Organ-on-a-Chip Platforms: A Systematic Review, *Sensors*, 2021, **21**(9), 3304.

51 S. Leonhardt, M. Klare, M. Scheer, T. Fischer, B. Cordes and M. Eblenkamp, Biocompatibility of photopolymers for additive manufacturing, *Curr. Dir. Biomed. Eng.*, 2016, **2**(1), 113–116.

52 F. Zhu, T. Friedrich, D. Nugegoda, J. Kaslin and D. Wlodkowic, Assessment of the biocompatibility of three-dimensional-printed polymers using multispecies toxicity tests, *Biomicrofluidics*, 2015, **9**(6), 061103.

53 H. Chen, D. H. Cheng, S. C. Huang and Y. M. Lin, Comparison of flexural properties and cytotoxicity of interim materials printed from mono-LCD and DLP 3D printers, *J Prosthet Dent*, 2021, **126**(5), 703–708.

54 A. Zimmerling, C. Sunil, Y. Zhou and X. Chen, Development of a Nanoparticle System for Controlled Release in Bioprinted Respiratory Scaffolds, *J. Funct. Biomater.*, 2024, **15**(1), 20.

55 Y. Wang, Z. Li, J. Ouyang and G. E. Karniadakis, Controlled release of entrapped nanoparticles from thermoresponsive hydrogels with tunable network characteristics, *Soft Matter*, 2020, **16**(20), 4756–4766.

56 C. Gonçalves, P. Pereira and M. Gama, Self-Assembled Hydrogel Nanoparticles for Drug Delivery Applications, *Materials*, 2010, **3**(2), 1420–1460, DOI: **10.3390/ma3021420**, eCollection 2010 Feb.

57 Y. Zhang, H. Zhang, M. Wang, T. Schmid, Z. Xin, L. Kozhuharova, W.-K. Yu, Y. Huang, F. Cai and E. Biskup, Hypoxia in Breast Cancer—Scientific Translation to Therapeutic and Diagnostic Clinical Applications, *Front. Oncol.*, 2021, **11**, 652266.

58 S. Zhi, C. Chen, H. Huang, Z. Zhang, F. Zeng and S. Zhang, Hypoxia-inducible factor in breast cancer: role and target for breast cancer treatment, *Front. Immunol.*, 2024, **15**, 1370800.

59 F. T. Lee-Montiel, S. M. George, A. H. Gough, A. D. Sharma, J. Wu, R. DeBiasio, L. A. Vernetti and D. L. Taylor, Control of oxygen tension recapitulates zone-specific functions in human liver microphysiology systems, *Exp. Biol. Med.*, 2017, **242**(16), 1617–1632.

60 T. Kietzmann, E. Y. Dimova, D. Flügel and J. G. Scharf, Oxygen: modulator of physiological and pathophysiological processes in the liver, *Z. Gastroenterol.*, 2006, **44**(1), 67–76.

61 S. Ben-Moshe and S. Itzkovitz, Spatial heterogeneity in the mammalian liver, Nature Reviews, *Gastroenterol. Hepatol.*, 2019, **16**(7), 395–410.

62 J. R. Choi, K. W. Yong, J. Y. Choi and A. C. Cowie, Recent advances in photo-crosslinkable hydrogels for biomedical applications, *BioTechniques*, 2019, **66**(1), 40–53.

63 D. Loessner, C. Meinert, E. Kaemmerer, L. C. Martine, K. Yue, P. A. Levett, T. J. Klein, F. P. W. Melchels, A. Khademhosseini and D. W. Hutmacher, Functionalization, preparation and use of cell-laden gelatin methacryloyl–based hydrogels as modular tissue culture platforms, *Nat. Protoc.*, 2016, **11**(4), 727–746.

64 J. E. Ziello, I. S. Jovin and Y. Huang, Hypoxia-Inducible Factor (HIF)-1 regulatory pathway and its potential for therapeutic intervention in malignancy and ischemia, *Yale J. Biol. Med.*, 2007, **80**(2), 51–60.

65 A. Gomes, L. Guillaume, D. R. Grimes, J. Fehrenbach, V. Lobjois and B. Ducommun, Oxygen Partial Pressure Is a Rate-Limiting Parameter for Cell Proliferation in 3D Spheroids Grown in Physioxic Culture Condition, *PLoS One*, 2016, **11**(8), e0161239.

66 L. Rui, Energy metabolism in the liver, *Compr. Physiol.*, 2014, **4**(1), 177–197.

67 T. Kietzmann, Metabolic zonation of the liver: The oxygen gradient revisited, *Redox Biol.*, 2017, **11**, 622–630.

68 B. P. Chan and K. W. Leong, Scaffolding in tissue engineering: general approaches and tissue-specific considerations, *Eur. Spine J.*, 2008, **17**(Suppl 4), 467–479.

69 K. Ronaldson-Bouchard, K. Yeager, D. Teles, T. Chen, S. Ma, L. Song, K. Morikawa, H. M. Wobma, A. Vasciaveo, E. C. Ruiz, M. Yazawa and G. Vunjak-Novakovic, Engineering of human cardiac muscle electromechanically matured to an adult-like phenotype, *Nat. Protoc.*, 2019, **14**(10), 2781–2817.

70 S. S. Lee, X. Du, I. Kim and S. J. Ferguson, Scaffolds for bone-tissue engineering, *Matter*, 2022, **5**(9), 2722–2759.

71 J. Kim, I. U. Kim, Z. F. Lee, G.-D. Sim and J. S. Jeon, Strategic Approaches in Generation of Robust Microphysiological 3D Musculoskeletal Tissue System, *Adv. Funct. Mater.*, 2024, **34**(52), 2410872.

72 S. Cho and J. Jang, Recent Trends in Biofabrication Technologies for Studying Skeletal Muscle Tissue-Related Diseases, *Front. Bioeng. Biotechnol.*, 2021, **9**, 782333.

73 G. Agrawal, A. Aung and S. Varghese, Skeletal muscle-on-a-chip: an in vitro model to evaluate tissue formation and injury, *Lab Chip*, 2017, **17**(20), 3447–3461.

74 N. Rose, B. Estrada Chavez, S. Sonam, T. Nguyen, G. Grenci, A. Bigot, A. Muchir, B. Ladoux, B. Cadot, F. Le Grand and L. Trichet, Bioengineering a miniaturized in vitro 3D myotube contraction monitoring chip to model muscular dystrophies, *Biomaterials*, 2023, **293**, 121935.

75 H.-W. Kang, S. J. Lee, I. K. Ko, C. Kengla, J. J. Yoo and A. Atala, A 3D bioprinting system to produce human-scale tissue constructs with structural integrity, *Nat. Biotechnol.*, 2016, **34**(3), 312–319.

76 N. T. Saidy, F. Wolf, O. Bas, H. Keijdener, D. W. Hutmacher, P. Mela and E. M. De-Juan-Pardo, Biologically Inspired Scaffolds for Heart Valve Tissue Engineering via Melt Electrowriting, *Small*, 2019, **15**(24), e1900873.

77 A. Weekes, G. Wehr, N. Pinto, J. Jenkins, Z. Li, C. Meinert and T. J. Klein, Highly compliant biomimetic scaffolds for small diameter tissue-engineered vascular grafts (TEVGs) produced via melt electrowriting (MEW), *Biofabrication*, 2023, **16**(1), 015017.

78 R. J. Mills, D. M. Titmarsh, X. Koenig, B. L. Parker, J. G. Ryall, G. A. Quaife-Ryan, H. K. Voges, M. P. Hodson, C. Ferguson, L. Drowley, A. T. Plowright, E. J. Needham, Q. D.

Wang, P. Gregorevic, M. Xin, W. G. Thomas, R. G. Parton, L. K. Nielsen, B. S. Launikonis, D. E. James, D. A. Elliott, E. R. Porrello and J. E. Hudson, Functional screening in human cardiac organoids reveals a metabolic mechanism for cardiomyocyte cell cycle arrest, *Proc. Natl. Acad. Sci. U. S. A.*, 2017, **114**(40), E8372–E8381.

79 Y. Morimoto, S. Mori, F. Sakai and S. Takeuchi, Human induced pluripotent stem cell-derived fiber-shaped cardiac tissue on a chip, *Lab Chip*, 2016, **16**(12), 2295–2301.

80 C. Cvetkovic, R. Raman, V. Chan, B. J. Williams, M. Tolish, P. Bajaj, M. S. Sakar, H. H. Asada, M. T. Saif and R. Bashir, Three-dimensionally printed biological machines powered by skeletal muscle, *Proc. Natl. Acad. Sci. U. S. A.*, 2014, **111**(28), 10125–10130.

81 M. S. Sakar, D. Neal, T. Boudou, M. A. Borochin, Y. Li, R. Weiss, R. D. Kamm, C. S. Chen and H. H. Asada, Formation and optogenetic control of engineered 3D skeletal muscle bioactuators, *Lab Chip*, 2012, **12**(23), 4976–4985.

82 K. H. Alliband, T. Parr, P. H. Jethwa and J. M. Brameld, Active vitamin D increases myogenic differentiation in C2C12 cells via a vitamin D response element on the myogenin promoter, *Frontiers in Physiology*, 2024, **14**, 1322677.

83 H. Gao, J. Xiao, Y. Wei, H. Wang, H. Wan and S. Liu, Regulation of Myogenic Differentiation by Topologically Microgrooved Surfaces for Skeletal Muscle Tissue Engineering, *ACS Omega*, 2021, **6**(32), 20931–20940.

84 N. Sunildutt, P. Parihar, A. R. Chethikkattuveli Salih, S. H. Lee and K. H. Choi, Revolutionizing drug development: harnessing the potential of organ-on-chip technology for disease modeling and drug discovery, *Front. Pharmacol.*, 2023, **14**, 1139229.

85 S. H. Lee and J. H. Sung, Microtechnology-Based Multi-Organ Models, *Bioengineering*, 2017, **4**(2), 46.

86 A. B. Sanchez-Spitman, J. J. Swen, V. O. Dezentje, D. J. A. R. Moes, H. Gelderblom and H. J. Guchelaar, Clinical pharmacokinetics and pharmacogenetics of tamoxifen and endoxifen, *Expert Rev. Clin. Pharmacol.*, 2019, **12**(6), 523–536.

87 C. W. McAleer, C. J. Long, D. Elbrecht, T. Sasserath, L. R. Bridges, J. W. Rumsey, C. Martin, M. Schnepper, Y. Wang, F. Schuler, A. B. Roth, C. Funk, M. L. Shuler and J. J. Hickman, Multi-organ system for the evaluation of efficacy and off-target toxicity of anticancer therapeutics, *Sci. Transl. Med.*, 2019, **11**(497), eaav1386.

88 L. Neufeld, E. Yeini, S. Pozzi and R. Satchi-Fainaro, 3D bioprinted cancer models: from basic biology to drug development, *Nat. Rev. Cancer*, 2022, **22**(12), 679–692.

89 A. A. Bagdasaryan, V. N. Chubarev, E. A. Smolyarchuk, V. N. Drozdov, I. I. Krasnyuk, J. Liu, R. Fan, E. Tse, E. V. Shikh and O. A. Sukocheva, Pharmacogenetics of Drug Metabolism: The Role of Gene Polymorphism in the Regulation of Doxorubicin Safety and Efficacy, *Cancers*, 2022, **14**(21), 5436.

90 P. B. Desai, S. C. Nallani, R. S. Sane, L. B. Moore, B. J. Goodwin, D. J. Buckley and A. R. Buckley, Induction of Cytochrome P450 3A4 in Primary Human Hepatocytes and Activation of the Human Pregnane X Receptor by Tamoxifen and 4-Hydroxytamoxifen, *Drug Metab. Dispos.*, 2002, **30**(5), 608–612.

91 P. A. J. Speth, Q. G. C. M. van Hoesel and C. Haanen, Clinical Pharmacokinetics of Doxorubicin, *Clin. Pharmacokinet.*, 1988, **15**(1), 15–31.

92 L. C. Floren, M. F. Hebert, A. P. Venook, V. C. Jordan, A. Cisneros and K. A. Somberg, Tamoxifen in liver disease: potential exacerbation of hepatic dysfunction, *Ann. Oncol.*, 1998, **9**(10), 1123–1126.

93 P. L. Prasanna, K. Renu and A. V. Gopalakrishnan, New molecular and biochemical insights of doxorubicin-induced hepatotoxicity, *Life Sci.*, 2020, **250**, 117599.

94 G. Huskin, J. Chen, T. Davis and H. W. Jun, Tissue-Engineered 3D In Vitro Disease Models for High-Throughput Drug Screening, *Tissue Eng. Regener. Med.*, 2023, **20**(4), 523–538.

95 C. Vitale, M. Marzagalli, S. Scaglione, A. Dondero, C. Bottino and R. Castriconi, Tumor Microenvironment and Hydrogel-Based 3D Cancer Models for In Vitro Testing Immunotherapies, *Cancers*, 2022, **14**(4), 1013.

96 U. N. Lee, J. H. Day, A. J. Haack, R. C. Bretherton, W. Lu, C. A. DeForest, A. B. Theberge and E. Berthier, Layer-by-layer fabrication of 3D hydrogel structures using open microfluidics, *Lab Chip*, 2020, **20**(3), 525–536.

97 A. Rajeev, K. Kansara and D. Bhatia, Navigating the challenges and exploring the perspectives associated with emerging novel biomaterials, *Biomater. Sci.*, 2024, **12**(14), 3565–3581.

98 S. M. Grist, L. Chrostowski and K. C. Cheung, Optical oxygen sensors for applications in microfluidic cell culture, *Sensors*, 2010, **10**(10), 9286–9316.

99 N. Contessi Negrini, C. Ricci, F. Bongiorni, L. Trombi, D. D'Alessandro, S. Danti and S. Farè, An Osteosarcoma Model by 3D Printed Polyurethane Scaffold and In Vitro Generated Bone Extracellular Matrix, *Cancers*, 2022, **14**(8), 2003.

100 J. Zhang, D. Tong, H. Song, R. Ruan, Y. Sun, Y. Lin, J. Wang, L. Hou, J. Dai, J. Ding and H. Yang, Osteoimmunity-Regulating Biomimetically Hierarchical Scaffold for Augmented Bone Regeneration, *Adv. Mater.*, 2022, **34**(36), 2202044.

101 B. Gu, Q. Ma, J. Li, W. Xu, Y. Xie, P. Lu, K. Yu, Z. Huo, X. Li, J. Peng, Y. Jiang, D. Li and J. He, Multi-material Electrohydrodynamic Printing of Bioelectronics with Sub-Microscale 3D Gold Pillars for In Vitro Extra- and Intra-Cellular Electrophysiological Recordings, *Adv. Sci.*, 2025, e2407969.

102 C. Cofiño-Fabres, T. Boonen, J. M. Rivera-Arbeláez, M. Rijpkema, L. Blauw, P. C. N. Rensen, V. Schwach, M. C. Ribeiro and R. Passier, Micro-Engineered Heart Tissues On-Chip with Heterotypic Cell Composition Display Self-Organization and Improved Cardiac Function, *Adv. Healthcare Mater.*, 2024, **13**(18), 2303664.

103 M. Virumbrales-Muñoz, J. M. Ayuso, A. Lacueva, T. Randelovic, M. K. Livingston, D. J. Beebe, S. Oliván, D. Pereboom, M. Doblare, L. Fernández and I. Ochoa, Enabling cell recovery from 3D cell culture microfluidic devices for tumour microenvironment biomarker profiling, *Sci. Rep.*, 2019, **9**(1), 6199.

104 K. Ronaldson-Bouchard, D. Teles, K. Yeager, D. N. Tavakol, Y. Zhao, A. Chramiec, S. Tagore, M. Summers, S. Stylianos, M. Tamargo, B. M. Lee, S. P. Halligan, E. H. Abaci, Z. Guo, J. Jacków, A. Pappalardo, J. Shih, R. K. Soni, S. Sonar, C. German, A. M. Christiano, A. Califano, K. K. Hirschi, C. S. Chen, A. Przekwas and G. Vunjak-Novakovic, A multi-organ chip with matured tissue niches linked by vascular flow, *Nat. Biomed. Eng.*, 2022, **6**(4), 351–371.

105 C. Oleaga, C. Bernabini, A. S. T. Smith, B. Srinivasan, M. Jackson, W. McLamb, V. Platt, R. Bridges, Y. Cai, N. Santhanam, B. Berry, S. Najjar, N. Akanda, X. Guo, C. Martin, G. Ekman, M. B. Esch, J. Langer, G. Ouedraogo, J. Cotovio, L. Breton, M. L. Shuler and J. J. Hickman, Multi-Organ toxicity demonstration in a functional human in vitro system composed of four organs, *Sci. Rep.*, 2016, 20030.

106 M. A. M. Vis, K. Ito and S. Hofmann, Impact of Culture Medium on Cellular Interactions in in vitro Co-culture Systems, *Front. Bioeng. Biotechnol.*, 2020, **8**, 911.

107 C. Zhang, Z. Zhao, N. A. Abdul Rahim, D. van Noort and H. Yu, Towards a human-on-chip: Culturing multiple cell types on a chip with compartmentalized microenvironments, *Lab Chip*, 2009, **9**(22), 3185–3192.

108 T. Weber, J. Bajramovic and S. Oredsson, Preparation of a universally usable, animal product free, defined medium for 2D and 3D culturing of normal and cancer cells, *MethodsX*, 2024, **12**, 102592.

109 S. C. da Silva Rosa, N. Nayak, A. M. Caymo and J. W. Gordon, Mechanisms of muscle insulin resistance and the cross-talk with liver and adipose tissue, *Physiol. Rep.*, 2020, **8**(19), e14607.

110 B. Feng, J. Wu, B. Shen, F. Jiang and J. Feng, Cancer-associated fibroblasts and resistance to anticancer therapies: status, mechanisms, and countermeasures, *Cancer Cell Int.*, 2022, **22**(1), 166.

111 J. H. Sung, C. Kam and M. L. Shuler, A microfluidic device for a pharmacokinetic–pharmacodynamic (PK–PD) model on a chip, *Lab Chip*, 2010, **10**(4), 446–455.